

# REPORT DOCUMENTATION PAGE

AFRL-SR-AR-TR-09-0046

Public reporting burden for this collection of information is estimated to average 1 hour per response, including the time for reviewing instructions, data needed, and completing and reviewing this collection of information. Send comments regarding this burden estimate or any other aspect of this burden to Department of Defense, Washington Headquarters Services, Directorate for Information Operations and Reports (0704-0188), 1215 4302. Respondents should be aware that notwithstanding any other provision of law, no person shall be subject to any penalty for failing to comply with a collection of information if it does not have a valid OMB control number. PLEASE DO NOT RETURN YOUR FORM TO THE ABOVE ADDRESS.

1. REPORT DATE (DD-MM-YYYY) 08-28-2008		2. REPORT TYPE Final Report		3. DATES COVERED (From - To) 12-01-2005 to 11-30-2008	
4. TITLE AND SUBTITLE MIMO Radar: A Multi-Sensor, Spatially Diverse Radar  Architecture				5a. CONTRACT NUMBER	
				5b. GRANT NUMBER FA9550-06-1-0026	
				5c. PROGRAM ELEMENT NUMBER	
6. AUTHOR(S) Alexander M. Haimovich				5d. PROJECT NUMBER	
				5e. TASK NUMBER	
				5f. WORK UNIT NUMBER	
7. PERFORMING ORGANIZATION NAME(S) AND ADDRESS(ES)  New Jersey Institute of Technology University Heights Newark, NJ 07102				8. PERFORMING ORGANIZATION REPORT NUMBER	
9. SPONSORING / MONITORING AGENCY NAME(S) AND ADDRESS(ES) AFOSR - Dr. Jon Sjogren 875 N Randolph St Arlington, VA 22203				10. SPONSOR/MONITOR'S ACRONYM(S)	
				11. SPONSOR/MONITOR'S REPORT NUMBER(S)	
12. DISTRIBUTION / AVAILABILITY STATEMENT  Distribution A: Approved for public release					
13. SUPPLEMENTARY NOTES					
14. ABSTRACT The research supported by this grant: (a) provides an in depth analysis of the localization accuracy gain attainable with the MIMO radar systems by means of the Cramer-Rao Lower bound (b)introduces the geometric dilution of precision (GDOP) metric and the contour mapping, providing an insight into the relative performance accuracy for a given layout of radars over a given geographic area. These plots offer a clear understanding of the collaboration effect of different sensor scheme on the resulting accuracy. Furthermore, target localization estimators were developed and evaluated (c)presents the analysis on the ambiguity arising in the high resolution localization due to side-lobe characteristics of the MIMO system and viable solutions to the problem. This report documents our work on MIMO radar with widely separated antennas thus called ``distributed MIMO radar''. Widely separated transmit/receive antennas capture the spatial diversity of the target's radar cross section (RCS). For target location, it is shown that coherent processing can provide a resolution far exceeding that supported by the radar's waveform.					
15. SUBJECT TERMS					
16. SECURITY CLASSIFICATION OF:			17. LIMITATION OF ABSTRACT	18. NUMBER OF PAGES	19a. NAME OF RESPONSIBLE PERSON
a. REPORT	b. ABSTRACT	c. THIS PAGE			19b. TELEPHONE NUMBER (include area code)

# MIMO Radar: A Multi-Sensor Spatially Diverse Radar Architecture

Air Force Office of Scientific Research grant no. FA9550-06-1-0026

Final Report - Dec. 1, 2005 - Nov. 30, 2008

Alexander M. Haimovich

August 28, 2008

## Abstract

The Air Force Office of Scientific Research supported the research on MIMO radar carried out at the New Jersey Institute of Technology during the period from December 2005 to November 2008 under the agreement number FA9550-06-1-0026. The purpose of this report is to summarize the proceedings and findings of the studies supported by this agreement. Starting with a short introduction, this report provides an overview of the research results on distributed MIMO radar with respect to localization accuracy gain and techniques, ambiguity resolution techniques, and waveform design. MIMO (multiple-input multiple-output) radar refers to an architecture that employs multiple, spatially distributed transmitters and receivers. While, in a general sense, MIMO radar can be viewed as a type of multistatic radar, the separate nomenclature suggests unique features that set MIMO radar apart from the multistatic radar and establishes close relation to MIMO communications. This report documents our work on MIMO radar with widely separated antennas thus called "distributed MIMO radar". Widely separated transmit/receive antennas capture the spatial diversity of the target's radar cross section (RCS). Unique features of MIMO radar are explained and illustrated by examples. It is shown that with non-coherent processing, a target's RCS spatial variations can be exploited to obtain a diversity gain for target detection and for estimation of various parameters, such as angle of arrival and Doppler. For target location, it is shown that coherent processing can provide a resolution far exceeding that supported by the radar's waveform.

The research supported by the grant: (a) provides an in depth analysis of the localization accuracy gain attainable with the MIMO radar systems by means of the Cramer-Rao Lower bound [1] (b) introduces the geometric dilution of precision (GDOP) metric and the contour

mapping [2], [3] providing an insight into the relative performance accuracy for a given layout of radars over a given geographic area. These plots offer a clear understanding of the collaboration effect of different sensor scheme on the resulting accuracy. Furthermore, target localization estimators were developed and evaluated [1]. (c) present the analysis on the ambiguity arising in the high resolution localization due to sidelobe characteristics of the MIMO system and viable solutions to the problem

## 1 Introduction

Active arrays, applied to radar systems, have been a topic of intensive research, and are well documented in the literature from the system implementation point of view (see survey of phased array systems in [4]), and in terms of processing techniques for target detection and parameter estimation [5]. Target parameters of interest in radar systems include target strength, location, and Doppler characteristics.

Phased-array radars with digital beamforming at the receiver have the ability to steer multiple, simultaneous beams (see, for example, [5, 6, 7]). Adaptive array radars process the signals received at the array elements in order to optimize some performance figure of merit, e.g., signal-to-interference ratio [8]. In airborne and other applications, the detection of moving targets and their discrimination against the background clutter are of great interest; this led to the development of array radars with space-time adaptive processing (STAP) [9, 10] (as well as recent books [11, 12]). In addition to spatial (or space-time) beamforming, signals received at an array can be processed to yield high resolution estimates of angle of arrivals of radar targets e.g., MUSIC or maximum likelihood (ML) [5].

Phased-arrays with multiple transmit elements are capable of cohering and steering the transmitted energy [7]. Elements of phased-array radars are typically co-located, both at the transmitter and receiver ends. Multiple transmit antennas suitably placed may be configured to operate in multistatic mode. Typically, a multistatic radar is a system that networks multiple, independent radars. Each radar performs a significant amount of local processing. Outcomes of the local processing are delivered to a central processor through a communication link [13]. For example, individual radars of a multistatic system perform local detection decisions, leaving the central processor the task of fusing these decisions.



In the 1990's, a new and interesting concept, employing multiple transmit elements, has been introduced - synthetic impulse and aperture radar (SIAR) [14]. The SIAR transmitting array emits orthogonal waveforms. This property ensures that a receiver that processes the aggregate of the transmitted waveforms is capable of separating and processing the waveforms individually. Through synthetic pulse formation, SIAR achieves the advantages of wideband radar (improved range resolution) but with individual antennas transmitting only narrowband waveforms. Unlike conventional beamformers, SIAR features isotropic radiation (an advantage in terms of the probability of intercept of the radar waveform by a third party). This concept involves a higher degree of cooperation among the radar sites than typical multistatic radar systems. As such, it has parallels with multiple-input multiple-output (MIMO) systems in wireless communications, and subsequent publications have adopted the "MIMO radar" nomenclature for radar systems with cooperating transmitters [15, 16, 17, 18].

In this report, a MIMO radar is defined broadly as a radar system employing multiple transmit waveforms and having the ability to jointly process signals received at multiple receive antennas. Elements of MIMO radar transmit independent waveforms resulting in an omnidirectional beam-pattern or create diverse beampatterns by controlling correlations among transmitted waveforms [19]. A MIMO radar may be configured with its antennas co-located or widely distributed over an area. MIMO radar is an emerging concept, but it is already apparent that it has the potential to make important contributions to the radar field. In [16] it is observed that MIMO radar has more degrees of freedom than systems with a single transmit antenna. These additional degrees of freedom support flexible time-energy management modes [17], leading to improved angular resolution [20, 21], and improved parameter identifiability [22]. With widely separated antennas, MIMO radar has the ability to improve radar performance by exploiting radar cross section (RCS) diversity [23], handle slow moving targets by exploiting Doppler estimates from multiple directions [24], and support high resolution target location [25].

MIMO radar with widely separated antennas is the topic of this report. From a model point of view, widely separated antennas take advantage of the spatial properties of extended targets, while with co-located antennas, the target is modeled as a point with no spatial properties. Each configuration and model has its strengths and challenges. With co-located antennas, MIMO radars can mimic beamformers utilizing low probability of intercept (LPI) waveforms. Rather than fo-

cusing energy on a target, the transmitted energy is evenly distributed in space [15]. The loss of processing gain compared to conventional phased-array beamforming due to the uniform illumination is compensated by the gain in time, since a narrow beam does not need to be scanned [18]. MIMO spatial signatures in systems with co-located antennas can be exploited to estimate radar parameters (location, RCS) of multiple targets, but the ability to resolve targets is limited by the Rayleigh resolution limit of the transmit/receive arrays. Widely separated antennas support high resolution target location, and by focusing on the effect of the channel, create a link between MIMO radar and MIMO communications.

MIMO systems have led to a revolution in wireless communications [26]. Recent publications (for example, [23] and references therein) indicate that one can exploit similar ideas in radar, suggesting interesting cross-fertilization of ideas between MIMO communications and MIMO radar. For quite some time, it has been understood that radar targets provide a rich scattering environment yielding 5 to 20 dB target RCS fluctuations, as illustrated in Fig. 1. Such targets display essentially independent scattering returns when radiated from sufficiently different directions (see [23] for a mathematical illustration of this using a reasonable model). The premise of MIMO radar with widely separated antennas is that angular spread (RCS variations as a function of aspect) can be exploited to improve radar performance in a variety of ways. The parallel to MIMO communication is recognized in the similar roles that the transmission medium (channel) and target play in respectively, communication and radar. In other words, the target serves as the “channel” in the radar problem. For example, combining target returns resulting from independent illuminations yields a *diversity gain* akin to the diversity gain obtained in the communication problem over fading channels when the data is transmitted through independent channels. Diversity gains are well understood in communications [27]. In radar, the idea is that any individual look at the target might have a small amplitude return with a significant probability, but by increasing the number of looks, the probability that all the looks have small amplitude returns can be made arbitrarily small. In [28] and some other publications, the nomenclature *statistical* has been used for MIMO radars that exploit a target’s spatial diversity.

Diversity gain is only one of two key gains that MIMO communications can provide. The other gain is called *spatial multiplexing* [26]. Spatial multiplexing in MIMO communications expresses the ability to use the transmit and receive antennas to set up a multidimensional space for signaling.

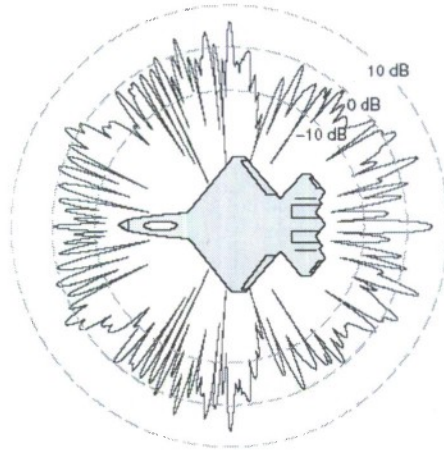


Figure 1: Backscatter as a function of azimuth.

Then, by suitable techniques, it is possible to form uncoupled, parallel channels that enable the rate of communication to grow in direct proportion to the number of such channels. Similarly, in MIMO radar, a multidimensional signal space is created when the returns from multiple scatterers or targets combine to generate a rich backscatter. With proper design, transmit-receive paths can be separated and exploited for improving radar performance.

In communications, the key property that made MIMO such a successful concept has been the ability to substitute the spatial dimension for the bandwidth resource. Narrowband MIMO communication systems perform like wideband systems without MIMO. In radar, bandwidth also plays an important role. Frequency diversity has been applied to decorrelate RCS response of complex targets, and high resolution location estimation is possible with wideband waveforms [29]. By exploiting the spatial dimension, MIMO radar with widely separated antennas may overcome bandwidth limitations and support high resolution target location. At the same time, this type of MIMO radar has the challenge of time and/or phase synchronizing multisite systems, and needs to deal with ambiguities stemming from the large separation between sensors.

This report elaborates the research proceedings on MIMO radar with widely separated antennas during the period from September 2005 till present with the goal of elucidating key concepts, illustrating them by examples, and thus encouraging further research on this emerging technology. Section 2 introduces the MIMO radar concept and discusses it in the context of other radar archi-

tectures. Analysis of the localization accuracy gain attainable with the MIMO radar systems by means of the Cramer-Rao Lower Bound and the geometric dilution of precision (GDOP) metric area are presented in Section 3. The contour mapping providing an insight into the relative performance accuracy for a given layout of radars over a given geographic area are presented in this section. Section 4 is devoted to discuss the findings on the ambiguity issues in localization arising out of sidelobe characteristics of MIMO system. Work done on solving this problem are presented therein. A discussion on the application of distributed MIMO radars is included in Section 5. Concluding remarks following in the last section. A comment on notation: vectors are denoted by lower-case bold, while matrices use upper-case bold letters. The superscripts ‘T’ and ‘†’ denote the transpose and Hermitian operators, respectively. Locations in the x-y plane are denoted in upper-case  $X = (x, y)$ .

## 2 MIMO Radar Concept

This section introduces the MIMO radar signal model, discusses conditions leading to RCS spatial diversity, and contrasts the architecture of MIMO radar with other multiple-element radars.

### 2.1 Signal Model

Assume a distributed target that consists of many, say  $Q$ , independent, isotropic scatterers located in a plane that also contains the transmit and receive antennas. The scatterers are located at coordinates  $X_q$ ,  $q = 1, \dots, Q$ , where  $X_q = (x_q, y_q)$ . Fig. 2 provides an illustration of the setup. In the figure, a distributed target is shown to comprise four scatterers. Each scatterer is represented by a circle to emphasize its isotropic reflectivity. The reflectivity of a scatterer is modeled by a zero-mean, independent and identically distributed (i.i.d.) complex random variable  $\zeta_q$  with variance  $E[|\zeta_q|^2] = 1/Q$ . Reflectivity values of the target are organized in a diagonal  $Q \times Q$  matrix,  $\Sigma = \text{diag}(\zeta_1, \dots, \zeta_Q)$ . Given the reflectivity of an individual scatterer, the target average RCS is  $E[\text{tr}(\Sigma\Sigma^\dagger)] = 1$ , independent of the number of scatterers in the model. If the RCS fluctuations are fixed during an antenna scan, but vary independently from scan to scan, our target model represents a classical Swerling case I (which represents a target in slow motion) [29]. Now let the target be illuminated by  $M$  transmitters arbitrarily located at coordinates  $T_k = (x_{tk}, y_{tk})$ ,



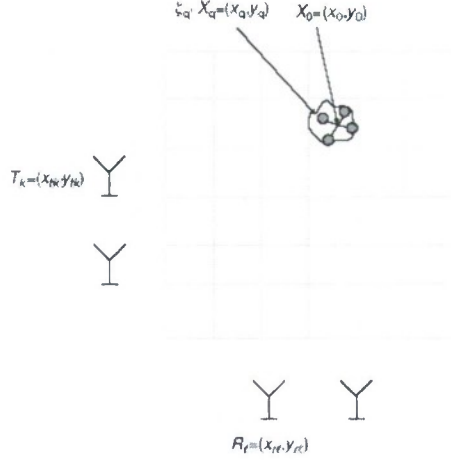


Figure 2: MIMO radar with extended target. Target comprises of four point scatterers. Scatterers located at points  $X_q$  and have reflectivity  $\zeta_q$ . RCS center of gravity located at  $X_0$ . Transmit antennas located at  $T_k$ , receive antennas located at  $R_\ell$ .

$k = 1, \dots, M$ . The signals scattered by the target are collected by  $N$  sensors placed at arbitrary coordinates  $R_\ell = (x_{r\ell}, y_{r\ell})$ ,  $\ell = 1, \dots, N$ . The set of transmitted waveforms in lowpass equivalent form is  $\sqrt{E/M}s_k(t)$ ,  $k = 1, \dots, M$ , where  $\int_{\mathcal{T}} |s_k(t)|^2 dt = 1$ ,  $E$  is the total transmitted energy, and  $\mathcal{T}$  is the waveforms' duration. Normalization by  $M$  makes the total energy independent of the number of transmitters. Let all transmitted waveforms have the same bandwidth  $W$ . Then the two-dimensional resolution cells illustrated by the grid in Fig. 2 have approximate dimensions  $(c/W) \times (c/W)$ , where  $c$  is the speed of light. Further specification of the waveforms  $s_k(t)$  depends on the application. For example, for focused beampatterns, the waveforms  $s_k(t)$  may be identical or differ by a phase shift. For target classification or parameter estimation, the statistical model for the observations may be employed for specialized waveform design [30]. In another example, for MIMO radar seeking to exploit target spatial diversity, it might be desired to design orthogonal waveforms, for ease of separation at the receiver. Orthogonality may be imposed in the time domain, frequency domain or in signal space. Throughout the paper it is assumed that transmitted waveforms are orthogonal and that orthogonality is maintained even for different mutual delays, i.e.,  $\int_{\mathcal{T}} s_k(t) s_m^*(t - \tau) dt = 0$  for all  $k \neq m$ , and for all time delays of interest.

In the model developed below, path loss effects are neglected, i.e., the model accounts for the



effect of the sensors/target locations only through time delays (or phase shifts) of the signals. It is not difficult to show that the lowpass equivalent of the signal observed at sensor  $\ell$  due to a transmission from sensor  $k$  and reflection from a scatterer at coordinates  $X_q = (x_q, y_q)$  (and excluding noise) is given by

$$z_{\ell k}^{(q)}(t) = \sqrt{\frac{E}{M}} \zeta_q s_k(t - \tau_{tk}(X_q) - \tau_{r\ell}(X_q)) \exp(-j2\pi f_c [\tau_{tk}(X_q) + \tau_{r\ell}(X_q)]), \quad (1)$$

where  $\tau_{tk}(X_q) = d(T_k, X_q)/c$  is the propagation time delay between the  $k$ -th transmitting sensor located at coordinates  $T_k$  and the scatterer at  $X_q$ ,  $d(T_k, X_q) = \sqrt{(x_{tk} - x_q)^2 + (y_{tk} - y_q)^2}$ , and  $f_c$  is the carrier frequency. The propagation time  $\tau_{r\ell}(X_q)$  from the scatterer to the  $\ell$ -th receiving sensor is defined analogously to  $\tau_{tk}(X_q)$ . Note that (1) denotes a near-field signal model, where the phase of the received signal is a function of the transmit and receive element locations as well as the location of the scatterer. In contrast, in a far-field signal model, the target is assumed to be sufficiently far such that it is essentially at the same distance and angle with respect to all the transmit and/or receive elements.

Continuing with the signal model in (1), we can interpret the term

$$h_{\ell k}^{(q)} = \zeta_q \exp(-j2\pi f_c [\tau_{tk}(X_q) + \tau_{r\ell}(X_q)]) \quad (2)$$

as the equivalent “channel” between transmitter  $k$ , scatterer  $q$ , and receiver  $\ell$ . A channel element (2) is comprised of three parts: (i)  $\exp[-j2\pi f_c \tau_{tk}(X_q)]$ , the phase shift due to the propagation from transmitter  $k$  to scatterer  $q$ , (ii)  $\zeta_q$ , the reflectivity of the scatterer, and (iii)  $\exp[-j2\pi f_c \tau_{r\ell}(X_q)]$ , the phase shift due to the propagation from the scatterer to receiver  $\ell$ . Summing over all the scatterers that make up the target, the model in (1) becomes

$$z_{\ell k}(t) = \sqrt{\frac{E}{M}} \sum_{q=1}^Q h_{\ell k}^{(q)} s_k(t - \tau_{tk}(X_q) - \tau_{r\ell}(X_q)). \quad (3)$$

We assume that the bandwidth of the transmitted waveforms is such that they are not capable of resolving individual scatterers. This is stipulated by the condition that the target has an RCS center of gravity at  $X_0 = (x_0, y_0)$ , and that  $s_k(t - \tau_{tk}(X_q) - \tau_{r\ell}(X_q)) \approx s_k(t - \tau_{tk}(X_0) - \tau_{r\ell}(X_0))$  for

all  $q = 1, \dots, Q$ . With this condition, (3) becomes

$$z_{\ell k}(t) = \sqrt{\frac{E}{M}} h_{\ell k} s_k(t - \tau_{tk}(X_0) - \tau_{r\ell}(X_0)), \quad (4)$$

where  $h_{\ell k} = \sum_{q=1}^Q h_{\ell k}^{(q)}$ .

The path gains  $h_{\ell k}$  from transmit to receive antennas of the MIMO radar are organized in a  $N \times M$  matrix  $\mathbf{H}$ . It can be shown that the matrix  $\mathbf{H}$  can be expressed [18]

$$\mathbf{H} = \mathbf{K}\mathbf{\Sigma}\mathbf{G}. \quad (5)$$

Equation (5) highlights the contribution of the transmit paths, the target components, and the receive paths: The transmit paths are represented by the  $Q \times M$  matrix  $\mathbf{G}$ ,  $\mathbf{G} = [\mathbf{g}_1^T; \mathbf{g}_2^T; \dots; \mathbf{g}_Q^T]$ ,  $\mathbf{g}_q^T = [1, \exp[-j2\pi f_c \tau_{t1}(X_q)], \dots, \exp[-j2\pi f_c \tau_{tM}(X_q)]]$ . Information on the receive paths is embedded in the  $N \times Q$  matrix  $\mathbf{K}$ ,  $\mathbf{K} = [\mathbf{k}_1, \mathbf{k}_2, \dots, \mathbf{k}_Q]$ , the semi-colon separates rows, and  $\mathbf{k}_q^T = [1, \exp[-j2\pi f_c \tau_{r1}(X_q)], \dots, \exp[-j2\pi f_c \tau_{rN}(X_q)]]$ . We recall that the matrix  $\mathbf{\Sigma}$  was defined in Section 2.1. From (4) and accounting for additive noise, it is possible to express the observed waveforms at the receive antenna  $\ell$  as:

$$r_\ell(t) = \sqrt{\frac{E}{M}} \sum_{k=1}^M h_{\ell k} s_k(t - \tau_{tk}(X_0) - \tau_{r\ell}(X_0)) + w_\ell(t), \quad (6)$$

where  $w_\ell(t)$  is circularly symmetric, zero-mean, complex Gaussian noise, spatially and temporally white with autocorrelation function  $\sigma_w^2 \delta(\tau)$ . We define the vector  $\mathbf{r}(t) = [r_1(t), \dots, r_N(t)]$  for later use. Properties of the elements  $h_{\ell k}$  of the channel matrix  $\mathbf{H}$  are discussed next.

## 2.2 Spatial Decorrelation

In the previous subsection, we introduced a stochastic model for the channel elements  $h_{\ell k}$ . Here, we discuss the conditions for spatial decorrelation of these elements.

In [23], it is shown that, if  $Q$  is large, all the channel elements  $h_{\ell k}$  are jointly Gaussian with zero mean and unit variance. Let two transmit antennas have coordinates  $(x_{tk}, y_{tk})$  and  $(x_{ti}, y_{ti})$ , respectively, and let the target dimensions along the  $x$  and  $y$  axes be  $D_x$  and  $D_y$ , respectively. Further, let two receive antennas have coordinates  $(x_{r\ell}, y_{r\ell})$  and  $(x_{rj}, y_{rj})$ , respectively. Recall

the definitions of distance  $d(T_k, X_0)$  between transmit antenna at  $T_k$  and the target at  $X_0$ , and of distance  $d(R_\ell, X_0)$  between receiver antenna at  $R_\ell$  and the target at  $X_0$ . If at least one of the following four conditions are met:

$$\begin{aligned}
x_{tk} - x_{ti} &> d(T_k, X_0) \lambda / D_x \\
y_{tk} - y_{ti} &> d(T_k, X_0) \lambda / D_y \\
x_{r\ell} - x_{rj} &> d(R_\ell, X_0) \lambda / D_x \\
y_{r\ell} - y_{rj} &> d(R_\ell, X_0) \lambda / D_y,
\end{aligned} \tag{7}$$

$$\begin{aligned}
\frac{x_{tk}}{d(T_k, X_0)} - \frac{x_{ti}}{d(T_i, X_0)} &> \frac{\lambda}{D_x} \\
\frac{y_{tk}}{d(T_k, X_0)} - \frac{y_{ti}}{d(T_i, X_0)} &> \frac{\lambda}{D_y} \\
\frac{x_{r\ell}}{d(R_\ell, X_0)} - \frac{x_{rj}}{d(R_j, X_0)} &> \frac{\lambda}{D_x} \\
\frac{y_{r\ell}}{d(R_\ell, X_0)} - \frac{y_{rj}}{d(R_j, X_0)} &> \frac{\lambda}{D_y}
\end{aligned}$$

where  $\lambda$  is the carrier wavelength, then it is shown in [23] that the  $\ell k$ -th and  $ji$ -th elements of the channel matrix are *uncorrelated*. Conversely, if

$$\begin{aligned}
x_{tk} - x_{ti} &\ll d(T_k, X_0) \lambda / D_x \\
y_{tk} - y_{ti} &\ll d(T_k, X_0) \lambda / D_y \\
x_{r\ell} - x_{rj} &\ll d(R_\ell, X_0) \lambda / D_x \\
y_{r\ell} - y_{rj} &\ll d(R_\ell, X_0) \lambda / D_y,
\end{aligned} \tag{8}$$

then the  $\ell k$ -th and  $ji$ -th elements of the channel matrix are *correlated*. Loosely speaking, these results mean that if the distributed target is viewed as an antenna with aperture length  $D$  ( $D$  could be  $D_x$  or  $D_y$  from the discussion above) the elements of the channel matrix  $\mathbf{H}$  decorrelate if the target's beamwidth cannot illuminate two sensors simultaneously. An illustration of this concept is shown in Fig. 3. For example, for a target at distance  $d = 10^4 \lambda$  and of dimension  $D = 10 \lambda$ , the separation required between the elements of the MIMO radar is of the order  $10^3 \lambda$ . Conversely, when

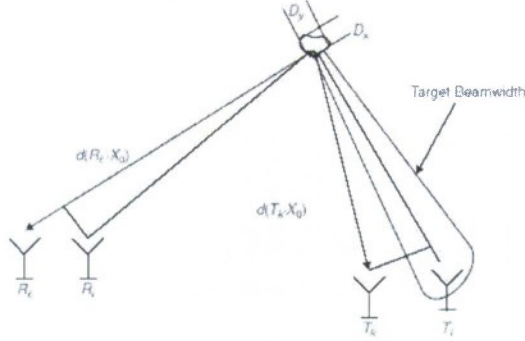


Figure 3: Elements of the channel matrix decorrelate when the MIMO radar antennas fall in different beamwidths originating from the target.

the distributed target acts as an antenna that has two sensors in the same beamwidth, elements of  $\mathbf{H}$  associated with these sensors are correlated. Since each element of  $\mathbf{H}$  represents the path gain of a transmitter-receiver pair, decorrelation supports a diversity of path gains. We conclude from the foregoing discussion that to obtain path diversity to an extended target, the MIMO radar antennas need to be sufficiently separated. However, even when the MIMO radar antennas are co-located, (left hand side terms in (7) are of the order of  $\lambda/2$ ), then decorrelation is still possible for large  $D$ . Taking the example we used earlier with a distance to target of  $d = 10^4\lambda$ , the condition for decorrelation is  $D > 2 \times 10^4\lambda$ , i.e., twice the distance to the “target”. In this case,  $D$  cannot be the aperture of a single extended target, but rather we could view *two* point targets separated by  $D$  as an array with two elements.

For further insight into the conditions for spatial decorrelation, let us consider the role of the target in the spatial decorrelation of the elements of  $\mathbf{H}$ . From the discussion so far, spatial decorrelation of the elements of the channel matrix occurs for complex targets (large number of scatterers  $Q$ ) and widely separated sensors. A large number of scatterers results in rich RCS patterns, such as the one in Fig. 1. The large number of scatterers, each with its own reflectivity  $\zeta_q$  and location  $X_q = (x_q, y_q)$ , combine at the receive sensors to create a fading signal. Widely spaced sensors cause the paths from the transmitters ( $T_k$ 's in Fig. 2) to the scatterers ( $X_q$ 's), and from the scatterers to the receivers ( $R_\ell$ 's) to be sufficiently diverse such that each receive sensor experiences a *different* fading signal. This is the root of the spatial decorrelation. What happens for simple targets with only a few scatterers? In the extreme of a single spherical scatterer with uniform RCS



as a function of angle, there are no multiple signals that combine to create the fading elements of the channel matrix. With the loss of fading, the elements of the channel matrix become correlated.

### 2.3 High Resolution Mode - Coherent Processing

It is useful at this point to review the time and phase synchronization requirements of the MIMO radar. For obtaining diversity gain in target detection the processing is non-coherent. The computation of the statistic requires the adjustment of time delays. This means that sensors need to have a common time reference, i.e., to be time synchronized. For instance in direction finding application, time synchronization is required between the widely distributed transmitters, while the receive end operates as a phased-array with inter-element spacing of  $\lambda/2$  and needs phase synchronization. Moving target detection requires time synchronization among sensors. In addition, each sensor is required to perform coherent time sampling.

We now turn to applications that require phase synchronization among widely separated sensors. Phase synchronization is required at both the transmit and receive ends. In the first example, we discuss high resolution target location. The second example is a brief discussion on the application of MIMO radar to estimate the number of targets.

We start by assuming a point target located at  $X_0 = (x_0, y_0)$ . The case of multiple targets will be discussed subsequently. From (6), we have

$$r_\ell(t) = \sqrt{\frac{E}{M}} \sum_{k=1}^M h_{\ell k} s_k(t - \tau_{tk}(X_0) - \tau_{r\ell}(X_0)) + w_\ell(t) \quad (9)$$

where the term  $h_{\ell k}$  is of the form (2), i.e.,  $h_{\ell k} = \zeta_0 \rho_{\ell k}(X_0)$ , and  $\rho_{\ell k}(X_0) = \exp[-j2\pi f_c(\tau_{tk}(X_0) + \tau_{r\ell}(X_0))]$ . The notation  $\rho_{\ell k}(X_0)$  emphasizes the dependency of the channel on the location of the target. The quantity  $\zeta_0$  represents the isotropic reflectivity of the target. Here, we assume that the target comprises a single scatterer, and that its reflectivity is  $\zeta_0$ . The reflectivity  $\zeta_0$  can be modeled as a random variable or as an unknown deterministic quantity. Following [25], the latter model is adopted for  $\zeta_0$ .

For high resolution target detection, we can set up a log-likelihood ratio test such as in (30), except that the likelihoods are calculated assuming the model for  $h_{\ell k}$  laid out in the previous paragraph. First, we develop the test statistic, then, we will demonstrate that the resolution

cells are of higher resolution than the detector. Under the  $H_1$  hypothesis, the likelihood function conditioned on the reflectivity  $\zeta_0$  and computed for a point  $X = (x, y)$  is given by

$$p_X(\mathbf{r}|H_1, \zeta_0) \propto \exp \left( -\frac{1}{\sigma_w^2} \sum_{\ell=1}^N \int_{\mathcal{T}} \left| r_{\ell}(t) - \zeta_0 \sqrt{\frac{E}{M}} \sum_{k=1}^M \rho_{\ell k}(X) s_k(t - \tau_{tk}(X) - \tau_{r\ell}(X)) \right|^2 dt \right). \quad (10)$$

The likelihood (10) is conditioned on  $\zeta_0$ . Keeping only terms that are dependent on the location  $X$

$$p_X(\mathbf{r}|H_1, \zeta_0) \propto \exp \left( -\frac{\sqrt{\frac{E}{M}}}{\sigma_w^2} \left[ |\zeta_0|^2 \sqrt{\frac{E}{M}} MN - 2 \operatorname{Re} \left( \zeta_0^* \sum_{\ell=1}^N \sum_{k=1}^M \rho_{\ell k}^*(X) y_{\ell k}(X) \right) \right] \right) \quad (11)$$

where  $\operatorname{Re}\{\cdot\}$  denotes the real part) and  $\mathbf{y}(X)$  is obtained by applying the matched filter for waveform  $s_k(t)$  to the received signal at the  $\ell$ -th antenna,  $r_{\ell}(t)$ , and sampling at a time delay corresponding to location  $X$ :

$$y_{\ell k}(X) = \int_{\mathcal{T}} r_{\ell}(t) s_k^*(t - [\tau_{tk}(X) + \tau_{r\ell}(X)]) dt. \quad (12)$$

To get rid of the nuisance parameter  $\zeta_0$ , its MLE is calculated and substituted back in (11). From (11), the MLE of  $\zeta_0$  is given by

$$\hat{\zeta}_0 = \frac{1}{\sqrt{\frac{E}{M}} MN} \sum_{\ell=1}^N \sum_{k=1}^M \rho_{\ell k}^*(X) y_{\ell k}(X).$$

Substituting back in (11) and dividing by  $p_X(\mathbf{r}|H_0) \propto \exp \left( -\frac{1}{\sigma_w^2} \sum_{\ell=1}^N \int_{\mathcal{T}} |r_{\ell}(t)|^2 dt \right)$ , it can be shown that the log-likelihood is given by

$$L_X(\mathbf{r}) \propto \left| \sum_{\ell=1}^N \sum_{k=1}^M \rho_{\ell k}^*(X) y_{\ell k}(X) \right|^2. \quad (13)$$

This expression must be evaluated by a central processor and it requires phase synchronization across both transmit and receive sensors. This is in contrast with the processing that extracts diversity gains or performs moving target detection, where the processing across sensors was non-coherent.

To obtain further insight into the high resolution mode, focus on the noiseless part of  $L_X(\mathbf{r})$ , and define the function

$$A(X) = \frac{1}{(MN)^2} \left| \sum_{\ell=1}^N \sum_{k=1}^M \rho_{\ell k}^*(X) \varphi_{\ell k}(X) \right|^2, \quad (14)$$

where

$$\varphi_{\ell k}(X) = \int_T s_k(t) s_k^*(t - \tau_{tk}(X) - \tau_{r\ell}(X)) dt. \quad (15)$$

The function  $A(X)$  represents the zero Doppler cut through the ambiguity function. The ambiguity function represents the response to a point target of reflectivity  $\zeta_0 = 1$  located at  $X_0$ , when the processing is adapted to a target located at  $X$ . The term  $\varphi_{\ell k}(X)$  is the ambiguity function (zero-Doppler cut) of the transmitted waveform measured at sensor  $\ell$ . Since  $A(X)$  requires phase information, it is referred to as the *coherent* ambiguity function of the MIMO radar. The high resolution properties of  $A(X)$  are determined by the phase terms  $\rho_{\ell k}(X) = \exp(j2\pi f_c[(\tau_{r\ell}(X) - \tau_{r\ell}(X_0))])$ . The *non-coherent* ambiguity function (assuming a point target) is given by

$$\begin{aligned} A_{nc}(X) &= \frac{1}{MN} \sum_{\ell=1}^N \sum_{k=1}^M |\rho_{\ell k}^*(X) \varphi_{\ell k}(X)|^2 \\ &= \frac{1}{MN} \sum_{\ell=1}^N \sum_{k=1}^M |\varphi_{\ell k}(X)|^2. \end{aligned} \quad (16)$$

It is clear that the values of the coherent ambiguity function are upper bounded by the non-coherent ambiguity function  $A(X) \leq A_{nc}(X)$ . The “coherent” ambiguity function  $A(X)$  is plotted in Fig. 4 for  $9 \times 9$  system and for the  $x$  coordinate. The “non-coherent” ambiguity function  $A_{nc}(X)$  is shown for comparison. The transmitters and receivers are placed uniformly in the sector  $-45^\circ$  to  $45^\circ$  with respect to the target. The ratio between the bandwidth and the carrier frequency is 0.01 (see [37] for more details). The high resolution capability is evident in the fact that the width of the mainlobe of the coherent ambiguity function is approximately equal in size to the wavelength  $\lambda$ , while the mainlobe of the non-coherent ambiguity function (determined by the bandwidth) is much wider.

The discussion above was concerned with a high resolution mode of MIMO radar applied to a point target. High resolution processing can also be applied to complex targets. Next, we

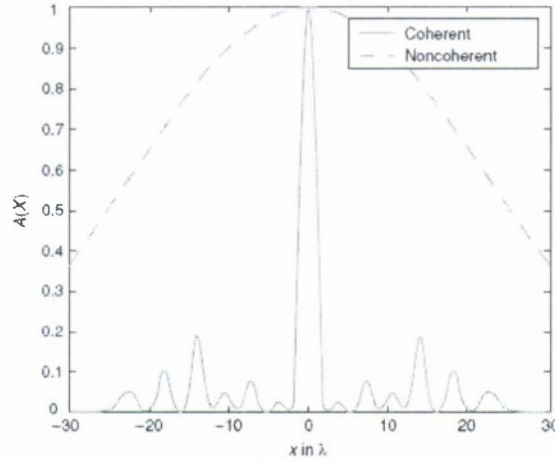


Figure 4: Coherent and noncoherent ambiguity functions for a 9 × 9 MIMO radar system.

demonstrate the ability of MIMO radar of resolving four targets located at coordinates  $(0, 0)$ ,  $(0, 6\lambda)$ ,  $(6\lambda, 0)$  and  $(6\lambda, 6\lambda)$ , respectively. Fig. 9 is a three-dimensional representation of the ambiguity function for four targets [37]. To compute the ambiguity function for this case, the first  $s_k(t)$  in (15) is substituted with  $\sum_{k=1}^4 s_k(t - \tau_{tk}(X_k) - \tau_{r\ell}(X_k))$ , where the  $X_k$ 's represent the targets' locations. The four scatterers are clearly visible.

The high resolution mode enabled by the coherent processing of widely distributed sensors merits further discussion. It is well known that given a linear array of length  $L$ , fully populated with sensors spaced at  $\lambda/2$  intervals, the cross-range resolution (the dimension parallel to the array) at distance  $d$  from the array is approximately  $\delta = d\lambda/L$ . Thinning the array preserves the resolution, but gives rise to grating lobes. Randomly placing the sensors of the thinned array breaks up the grating lobes at the cost of higher sidelobes than the fully populated array. Such arrays are referred to as *random arrays* and their properties have been investigated [38, 43]. Statistical analysis for a single transmitter and  $N$  receivers has shown that the mean sidelobe level (MSL) is approximately  $1/N$ . Our formulation of MIMO radar leading to (13) is consistent with an extension of the linear random array concept to a planar topology and multiple transmitters. The resolution of MIMO



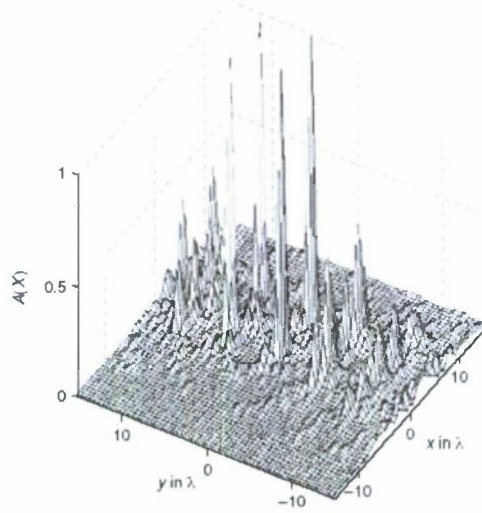


Figure 5: Coherent ambiguity function of a 9 × 9 MIMO radar for four targets.

radar configured with widely separated elements scales with the carrier wavelength  $\lambda$ , and thus, can greatly exceed the bandwidth resolution barrier set by the radar illuminating waveform.

With the higher resolution, the number of tests required for target detection may increase dramatically. An efficient mode of operation could be to let MIMO radar first detect the target over resolution cells  $(c/W) \times (c/W)$ . Once the presence of a target is determined, the MIMO radar will switch to high resolution mode seeking to extract additional information such as high resolution location, size, identification, etc.

While the MSL can be controlled through the number of elements in the array, more troubling from a performance point of view is the peak sidelobe level (PSL), which can exceed the MSL by 10 dB or more [38]. Controlling the MSL and PSL is of great interest in high resolution applications of MIMO radar. Maintaining coherency across sensors at both the transmit and receive ends results in a MSL of the order of  $1/(MN)$ . Note that a MIMO radar with full coherency requires  $(M + N)$  sensors to achieve the same MSL as a radar with one transmitter and  $MN$  receivers. MIMO radar thus has an economical advantage, since for cases of interest,  $(M + N) \ll MN$ .

A variety of techniques are available for reducing the PSL. Waveforms with frequency diversity

were suggested in [43]. Another idea first mentioned in the context of linear random arrays and that seems to have a natural extension to MIMO radar is the non-coherent combining of several random arrays [43].

**“Spatial Multiplexing” with MIMO Radar** Using the signal model developed in this section, the number of targets that can be handled simultaneously parallels the concept of “spatial multiplexing” in communications. The rank of the matrix  $\mathbf{H}$  defined in (5) is upper bounded by the lowest rank among the matrices  $\mathbf{K}$ ,  $\mathbf{\Sigma}$ , and  $\mathbf{G}$ . For sufficiently separated receive antennas, it can be shown that  $\text{rank} \mathbf{K} = N$  [18, 23]. Similarly, for sufficiently separated transmit antennas,  $\text{rank} \mathbf{G} = M$ . Finally, for  $Q$  point targets present,  $\text{rank} \mathbf{\Sigma} = Q$ . If  $Q \leq \min(M, N)$ , the rank of the matrix  $\mathbf{H}$  serves as an indicator of the number of targets in the field of view of the MIMO radar. An estimate of  $Q$  can be determined efficiently from a singular value decomposition of  $\mathbf{H}$  provided that the magnitudes of the singular values of the noise-plus-clutter are known to be much smaller than those corresponding to the signal returns.

### 3 Localization Accuracy

This section elaborates the analysis of the localization accuracy gain attainable with the MIMO radar systems by means of the Cramer-Rao Lower bound. Introducing the geometric dilution of precision (GDOP) metric and the contour mapping provides an insight into the relative performance accuracy for a given layout of radars over a given geographic area. These plots offer a clear understanding of the collaboration effect of different sensor scheme on the resulting accuracy. Furthermore, target localization estimators are developed and evaluated. The distinction between non-coherent and coherent applications relies on the need for merely time synchronization between the transmitting and receiving radars vs. the need for phase synchronization. The MIMO radar architecture with coherent processing exploits knowledge of the phase differences measured at the receive antennas to produce a high accuracy target location estimate. In traditional radar systems, bandwidth plays an important role in providing resolution range, i.e., it is inversely proportional to the signal efficient bandwidth. The ambiguity function concept has long been used in the context of localization. In [24] it has been used to provide a comparative performance of coherent vs. non-

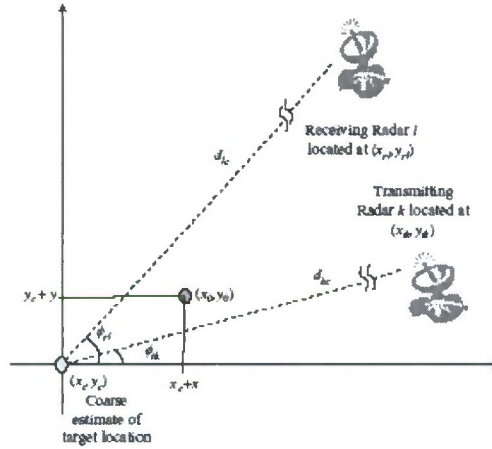


Figure 6: The MIMO radar linear perturbation model.

coherent processing of MIMO radar waveforms. The high accuracy localization benefits of coherent MIMO radar systems are inherent in the ambiguity function plots. As the potential for localization performance enhancement is evident from the ambiguity function, the lower bound on the attainable accuracy is set in [1] by developing the Cramer-Rao lower bound. The bound is shown to be proportional to the carrier wavelength squared, and independent of the signal bandwidth. It is also shown to be reliant on the location of the radars, although this dependency cannot be intuitively identified. For this, other tools need to be introduced, as we discuss later in the report. Once developing an expression for the lower bound on the MSE for target localization, we

turned our attention to target localization techniques and their performance relative to the CRLB. Two estimators were developed and presented in [1]: the maximum likelihood estimator (MLE) and the best linear unbiased estimator (BLUE). The MLE is motivated by its asymptotic optimality, while the BLUE by its closed form expression. The MLE is a practical estimator in the sense that its application to a problem of observations in white Gaussian noise is relatively straightforward. Moreover, under mild conditions on the probability density function of the observations,

the MLE of the unknown parameters is asymptotically unbiased, and it asymptotically attains the CRLB. Since a closed form expression cannot be found for the MLE, numerical methods need to be applied. A grid search or an iterative maximization of the likelihood function needs to be performed to determine the target location. This might involve a significant computational effort. A different approach to the problem is by using a linear perturbation model of the target location (as illustrated in Fig. 6) with the BLUE [1]. The BLUE estimator provides a closed form solution and a comprehensive evaluation of the performance of the estimators mean squared error (MSE). This result supports the expectation for the target localization accuracy to be independent of the bandwidth and provides an insight into the relation between sensors locations, target location, and localization accuracy. To establish a more comprehensive expression of these relations, a metric widely used in Global Positioning Systems (GPS) for mapping estimation precision and known as geometric dilution of precision (GDOP) was introduced in [1], [2].

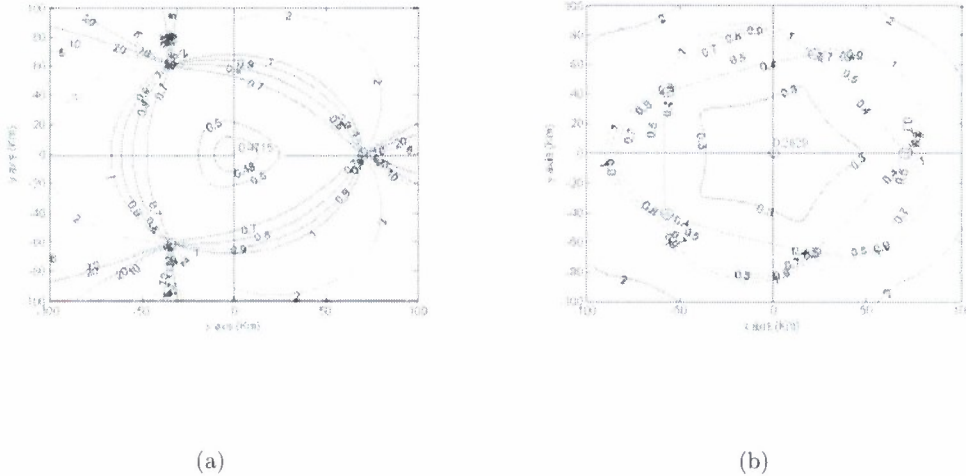


Figure 7: GDOP maps for a symmetric positioning of radars around the axis origin: case (a) for  $M = N = 3$  (b) for  $M = N = 5$ .

The GDOP metric expresses the effect of the positions of the transmitting and receiving elements of the MIMO radar on the relationship between the time delay estimation errors and the localization errors. In this expression, the sensors' locations are embedded. The GDOP reduces the combined effect of the locations to a single metric. Once we get the values mapped, the actual localization



error is easily derived by multiplying the GDOP value with a constant equal to the effect of the noise variance. In Fig. 13, contour plots of the GDOP values are presented for the case of respectively,  $M = N = 3$  and  $M = N = 5$  radars positioned symmetrically on the  $N$  vertices of a polygon centered at the origin. The radars are all transmitting orthogonal signals and perform time delay estimations. The first noticeable factor in the comparison of the two plots is the higher accuracy obtained with five radars compared to three radars. For example, the lowest GDOP value for the case of three radars is 0.4715, while with five radars, the GDOP is 0.2829, corresponding to a 60% improvement. All the targets located inside the virtual  $N$ -sided polygon achieve relative high accuracy localization, while the most accurate localization is obtained for the target at the center. The increase in GDOP values from the center to the polygon boundaries is slow. Outside this polygon, the GDOP values increase rather rapidly. In Fig. 8 contours of five non-symmetrically positioned radars are drawn. When the radars are spread around the target (Fig. 8(a)), there are still some areas with good measurement accuracy, though the coverage is shrunk compared to the case with symmetrical distribution of sensors in Fig. 7(b). When the viewing angle of the target is very restricted, as in Fig. 8(b), there is a marked degradation of GDOP values.

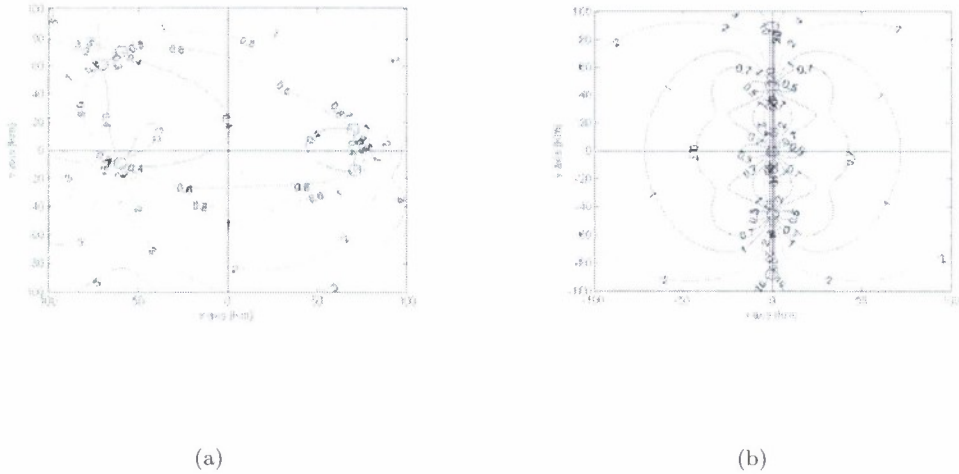


Figure 8: GDOP maps for a asymmetric positioning of radars around the axis origin: case (a) GDOP contours for an asymmetric positioning of radars around the axis origin. (b) GDOP contours for the case where the radar are aligned.

These examples have shown that a symmetrical deployment of sensors around the target yield

lowest GDOP values. Theoretical analysis of the lowest attainable GDOP for a passive system (such as GPS) is known to be  $2/\sqrt{M}$ , where  $M$  is the number of transmitting sensors. For MIMO radar system with  $M$  transmitters and  $N$  receivers, we have shown that the lowest achievable GDOP can be approximate by  $\sqrt{2/MN}$ , where for  $M = N$  it is equal to  $\sqrt{2/N^2}$ . This result is interpreted as a "MIMO advantage" compared to the single transmit antennas case. As a numerical example, the lowest GDOPs in Fig. 13 are respectively  $\sqrt{2/3^2} = 0.4715$  and  $\sqrt{2/5^2} = 0.2829$ . In summary, the work supported by this grant not only validated previous findings for the potential high accuracy performance of MIMO radar, but also resulted in new tools for target localization. We have developed analytical expressions for the estimation errors of coherent MIMO radar. It disclosed the dependency of the accuracy on the carrier wavelength and shows that MIMO radar can locate targets with high resolution. Practical localization tools like the MLE and the BLUE were attained. Study tools like the GDOP plots were developed to provide a clear view of high accuracy areas for a given set of radar locations. These plots could also serve as a decision supporting tool for choosing favorable radar locations to cover a given target area with high accuracy. The work supported by this grant has already served as a foundation of other scientistsf research, which underlines its innovative nature and significance.

## 4 Sidelobe Ambiguity

One of issues in distributed MIMO radar is the ambiguity in target localization due to the sidelobes in the spatial patterns of performance matrices. Coherent processing implies time synchronization at a finer scale for phase coherency in the received signal at receive antennas in addition to the delay compensation for the waveform at the matched filter receiver. To elaborate further, consider the scenario depicted in Fig. 9. A signal waveform transmitted from antenna  $k$  at the location  $P$  is reflected off by the target at the location  $O$  (observation point) and received by the antenna  $l$  at  $Q$ . In the process of scanning a point  $R$  in the surveillance area, the phase change due to the round trip path  $P - R - Q$  is compensated by the transmitter, or the receiver, or by both. When the scanning point  $R$  coincides with the actual location of the target  $O$ , phase change is perfectly compensated.

When the scanning point  $P$  is different from the actual location of the target  $O$ , the difference

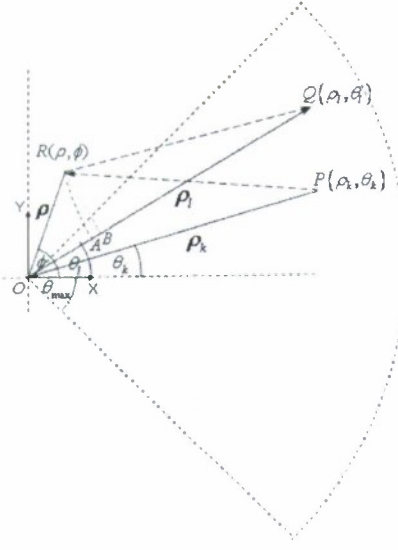


Figure 9: Analytical framework.

between the actual phase of the received signal and the computed phase, leads to under/over compensation of phase. The receiver output therefore is periodic over the space with the deviation of the scanning point from the actual location of the target. With multiple transmit and receive antennas, the phase compensation and the subsequent combining of receiver outputs amount to summing a number of vectors with different phases. When the scanning point coincides with the actual location of the target, complete coherency is achieved for all the transmit/receive antenna pairs and the resultant signal is maximized. At other locations, different transmit/receive antenna pairs experience different levels of phase coherency. The resultant signal thus forms a pattern with peaks and valleys over the two dimensional space of the surveillance area. We call the pattern in the space as the *random phase coherence ambiguity (RPCA) function*.

Ideally, we wish to have the RPCA pattern to be an impulse at  $O$ . Such an ideal pattern would let us have infinite resolution power resulting in ideal localization and imaging capabilities. The inherent nature of antenna arrays cause non-ideal behavior in several different ways. First, the resolution power is limited by the carrier frequency and the antenna aperture. In particular, for linear arrays, the beamwidth (defined in some sense, such as half-power or null-to-null) of the mainlobe is proportional to  $\lambda/L$ , where  $\lambda$  is the carrier wavelength and  $L$  is the aperture size of the antenna system [39]. While this result remains true for far-field as well as near-field scenarios, the

distributed MIMO radar adds another twist referred to as geometric dilution of precision (GDOP). GDOP is a term used in geo-positioning systems (GPS) to describe the effect of sensor location on the localization performance. The GDOP effect causes the beamwidth of the *mainlobe* of the RPCA pattern to depend on the geometry of the aperture as well. Best resolution is shown to be achieved when the antennas are placed symmetrically around the target [40, 41]. The second non-ideality is due to the sidelobe and grating lobe patterns. Grating lobes may have equal level as the main lobe, and the number of grating lobes appearing in the visible region (surveillance area) is a function of number of antennas and the aperture size. It has been shown that for an array of equally spaced elements, the number of grating lobes in the visible region reduces as the number of elements is increased. Nevertheless the grating lobes can be broken by randomizing the element positions, thus making it possible to reduce the number required elements to overcome the ambiguity due to grating lobes [38]. Distributed MIMO radars inherently have randomly distributed antennas and therefore, a study on the effect of randomness of elements on the ambiguity performance is of great interest.

In the process of target localization, a carrier modulated waveform is transmitted by each transmit antenna and received by all receive antennas. The waveforms are assumed to be mutually orthogonal. Thus with proper synchronization, each waveform can be separated out by correlating the received signal with each transmitted waveform. In the coherent processing approach, the receiver also uses carrier phase information. When the scanning point coincides with the actual target, perfect phase matching is achieved thus the received signal power is maximized. The effect of waveform is such that it behaves as an envelope to the sidelobes and grating lobes thus reducing the ambiguities. Nevertheless, the discussion in this proposal does not consider the waveforms. Rather, we study the effect of only the carrier phase. Therefore it is an analysis of worst case scenario with respect to the ambiguities in distributed MIMO radars.

**Maximum Likelihood Estimation and the RPCA Function** The concept of likelihood function and resulting RPCA function are described here so as to setup the background for the discussion to follow. Assume there are  $M$  transmit antennas and  $N$  receive antennas. A transmit antenna  $k$  transmits a waveform  $s_k(t) = s_k^b(t)e^{j2\pi f_0 t}$ , where  $s_k^b(t)$  is the equivalent lowpass signal waveform as a function of time  $t$ , and  $f_0$  is the carrier frequency. The received signal at transmitter



$l$  due to the transmission from  $k$  can be expressed as  $r_l(t) = \sum_{k=1}^M s_k(t - \tau_{kl}) + n_l(t)$ , where  $\tau_{kl}$  is the round-trip delay from  $k$  to  $l$  via the target and  $n_l(t)$  is the noise waveform at the receive antenna. We may express  $r_l(t)$  as  $r_l^b(t)e^{j2\pi f_0 t}$  in terms of the lowpass equivalent. With the assumption that the waveforms transmitted from two antennas say  $k$  and  $k'$  are mutually orthogonal for all delays, i.e.,  $\int s_k^b(t)s_{k'}^{b*}(t - \tau)dt \approx 0$  for all  $\tau$  and  $k \neq k'$ , the receiver  $l$  is able to separate out the waveforms transmitted from different antennas using the correlation process. The probability density function (pdf) of the received signal vector  $\mathbf{r}$  can be written as

$$f(\mathbf{r}) = \kappa \exp \left\{ -\frac{1}{\sigma^2} \sum_{k=1}^M \sum_{l=1}^N \int_{-\infty}^{\infty} |r_l(t) - \zeta \sum_{k=1}^M s_k(t - \tau_{kl})|^2 dt \right\}, \quad (17)$$

where  $\kappa$  is a proportionality constant,  $\sigma$  is the standard deviation of Gaussian noise, and  $\zeta$  is the reflection coefficient of the scatterer, assumed to be constant with respect to all transmit/receive antenna pairs. Expansion of (17) and the use of maximum likelihood criteria to eliminate  $\zeta$ , leads to the log-likelihood function that assigns values to an estimated location  $\xi$  with estimated delay  $\hat{\tau}_k$ :

$$\ln f(\mathbf{r}|\xi) = c_1 \left| \sum_{k=1}^M \sum_{l=1}^N e^{-j2\pi f_0 \tau_\xi} \int r_l^{b*}(t) s_k^b(t - \hat{\tau}_{kl}) dt \right|^2 + c_2, \quad (18)$$

where  $c_1$  and  $c_2$  are constants and  $\tau_\xi = \hat{\tau}_{kl} - \tau_{kl}$  is the *relative round trip delay* for the estimated location with respect to the actual location of the targets. The *ambiguity function* defined as a scaled version of log likelihood function in (18).

$$A(\xi) = \frac{1}{MN} \left| \sum_{k=1}^M \sum_{l=1}^N e^{-j2\pi f_0 \tau_\xi} \varphi_{s_k^b}(\hat{\tau}_{kl}) \right|. \quad (19)$$

where  $\varphi_{s_k^b}(\hat{\tau}_{kl}) = \int r_l^{b*}(t) s_k^b(t - \hat{\tau}_{kl}) dt$ . The ambiguity function defined here has been normalized such that in the absence of noise, the peak value is obtained at the actual location of the target. Our present work is concerned with the effect of phase coherency in the ambiguity function. Therefore with the omission of the effect of noise, and the assumption of unit energy for the waveform, we arrive at the RPCA function defined as

$$\mathcal{A}(\xi) = \frac{1}{MN} \sum_{k=1}^M \sum_{l=1}^N e^{-j2\pi f_0 \tau_\xi} \quad (20)$$

The absolute value notation  $|\cdot|$  is also omitted so that to leave  $\mathcal{A}(\xi)$  to be a function with magnitude and phase resulting in a function having correspondence to the antenna radiation patterns in the theory of random arrays. The high accuracy localization benefits of coherent MIMO radar systems are inherent in the ambiguity function plots, as it is the ability to distinguish between closely spaced multiple targets.

**Relation to the Theory of Random Arrays** With reference to Fig. 9 and the RPCA function defined in (20), the relative delay  $\tau_\xi$  is the delay corresponding the difference between round trip path lengths  $P - R - Q$  and  $P - O - Q$ . This difference is the sum of difference between the path segments  $\overline{PR}$  and  $\overline{PO}$  and the difference between path segments  $\overline{RQ}$  and  $\overline{OQ}$ . For a close examination of the parameters involved, consider the path  $RQ$  between scanning point  $R$  and the location of receive antenna  $Q$ . The difference between lengths of path segments  $\overline{RQ}$  and  $\overline{OQ}$  is equal to  $OA$  where the arc  $RA$  is drawn with center  $Q$  and radius  $QR$ . Thus the relative delay for the receive antenna  $l$  is given by  $\tau_{\xi l} = \frac{-OA}{c}$  where  $c$  is the speed of light. The distance from the scanning location to the location of receive antenna,  $RQ$  can be calculated in terms of the polar coordinates of locations  $R$  and  $Q$  by applying Pythagorous theorem. Thus we have  $OA = OQ - RQ = \rho_l \left[ 1 - \sqrt{1 - \left( \frac{2\rho}{\rho_l} \cos(\phi - \theta_l) - \frac{\rho^2}{\rho_l^2} \right)} \right]$ , where the coordinates of scanning location  $R$  are  $(\rho, \phi)$  and the coordinates of receive antennal location  $Q$  are  $(\rho_l, \theta_l)$ . Binomial expansion of the square root term and omission of higher order terms leads to the approximation  $OA \approx \rho \cos(\phi - \theta_l) - \frac{\rho^2}{2\rho_l}$ . When  $\rho \ll \rho_l$  the second order term can be omitted thus  $OA \approx \rho \cos(\phi - \theta_l)$ . In Fig. 9, this implies  $OA \approx OB$  where  $RB$  is perpendicular to  $OQ$ . It is seen that the relative delay in this case becomes dependent only on the bearing angle of the antenna with respect to  $O$ .

Nevertheless, as far as the complete MIMO system is concerned, the aperture of the entire deployment is comparable to the mean distance to the scatterer and therefore each antenna is seen with significantly different bearing angle. Therefore we have a near-field scenario with respect to the distributed MIMO system. This scenario is different from far-field radiation pattern encountered in the theory of random arrays. In the limiting case when the distance to the scatterer is much larger than the aperture size, the scenario becomes similar to that of random arrays. This transformation is illustrate in Fig. 10. With the completely far field scenario as in Fig. 10(b), the set of randomly placed antennas in the two dimensional space can be represented by two mutually orthogonal one

dimensional random arrays. Nevertheless, a framework more appropriate for the typical parameter setting in distributed MIMO radar is as in Fig. 10(a).

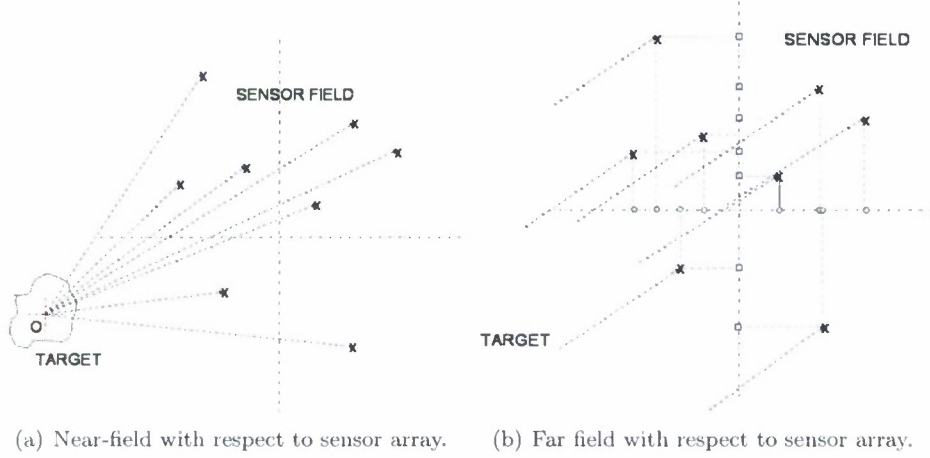


Figure 10: Near-field/far-field scenarios in distributed MIMO radar.

In our analytical framework, the distance is measured in wavelengths and the speed is measured in number of wavelengths per second. Thus the delay is equal to distance in value and therefore  $c$  and  $f_0$  can be dropped in the writing. The RPCA function can now be rewritten as

$$\mathcal{A}(\xi) = \frac{1}{MN} \sum_{k=1}^M \sum_{l=1}^N e^{-j2\pi\rho(\cos(\phi-\theta_k)+\cos(\phi-\theta_l))}. \quad (21)$$

When the scanning point coincides with the observation point, we have  $\mathcal{A}(P \equiv O) = 1$ . Outside of the neighborhood of  $O$ , the unit vectors  $e^{-j2\pi\rho(\cos(\phi-\theta_k)+\cos(\phi-\theta_l))}$  combine with random phases to produce a pattern with peaks and valleys in the two dimensional space.

As the potential for localization performance enhancement is evident from the ambiguity function, the lower bound on the attainable accuracy is set in [40] by developing the Cramer-Rao lower bound for target localization. The bound is shown to be inversely proportional to the *carrier wavelength*, and for narrowband signals, essentially independent of the signal bandwidth. Additionally, the CRLB on the target localization accuracy offers a *MIMO advantage* gain of the order of  $\sqrt{MN}$  (where  $M$  is the number of transmitting radars and  $N$  is the number of receiving radars) in the sense that the CRLB decreases with  $1/\sqrt{MN}$ . This outcome is consistent with the *diversity gain* in a MIMO communication system with  $M$  transmit and  $N$  receive antennas, where the maximal diversity gain is  $MN$ , which is the total number of fading gains that one can average over.

**Statistics of the RPCA function** In this section, the statistics of the RPCA function are examined. As the sensors in a distributed MIMO radar are randomly deployed, the RPCA is a random function in the two dimensional space. The distribution of peaks of RPCA outside of main beam over the surveillance area, or at the least, characterization of parameters such as first and second moments (mean and variance) as a function of spatial coordinates are of interest. Let  $u = \cos(\phi - \theta_k)$  and  $v = \cos(\phi - \theta_l)$ . Here  $\theta_k$  and  $\theta_l$  are random variables. Therefore for a given  $\phi$ ,  $u$  and  $v$  are random variables. Thus we rewrite (21) as

$$\mathcal{A}(\rho, \phi) = \frac{1}{MN} \sum_{k=1}^M \sum_{l=1}^N e^{-j2\pi\rho(u+v)}. \quad (22)$$

Assume that the antennas are uniformly distributed within a sector of angle  $2\theta_{max}$  with respect to the true position of the target, as shown in Fig. 9, leading to uniform distribution for  $\theta_k$  and  $\theta_l$  in  $[-\theta_{max}, \theta_{max}]$ . The probability density function of  $u$  (and  $v$ ) is given by  $f(u) = \frac{1}{2\theta_{max}\sqrt{1-u^2}}$ . We first discuss the behavior of the mean and the variance of  $P(\rho, \phi)$ . Next, the joint distribution of independent sample points in the sidelobe region is analyzed to obtain the requirements to achieve a given maximum guaranteed sidelobe level with a given confidence level within the surveillance region.

**Mean and Variance** The mean pattern is found by taking the expectation  $E[\mathcal{A}(\rho, \phi)]$  over  $u$  and  $v$  and is found to be

$$E[\mathcal{A}(\rho, \phi)] = \psi^2(\rho, \phi),$$

where  $\psi(\rho, \phi)$  is the characteristic function of  $u$  which can be shown to be given by

$$\psi(\rho, \phi) = \frac{1}{2\theta_{max}} \int_{\cos(\phi+\theta_{max})}^{\cos(\phi-\theta_{max})} \frac{e^{-j2\pi\rho u}}{\sqrt{1-u^2}} du. \quad (23)$$

Each quadrature component of  $\mathcal{A}(\rho, \alpha)$  in (22) is a summation of independent and identically distributed complex-valued random variables. Assuming that the number of terms in the sum is sufficient for the central limit theorem to apply, it is concluded that  $\mathcal{A}(\rho, \phi)$  has a complex Gaussian distribution. The variances of the real and imaginary parts of  $\mathcal{A}(\rho, \phi)$ ,  $\sigma_1^2(\rho, \alpha)$  and  $\sigma_2^2(\rho, \phi)$  respectively, can be derived with the steps as in [42]. It can be shown that the total



variance  $\sigma^2(\rho, \phi) = \sigma_1^2(\rho, \phi) + \sigma_2^2(\rho, \phi)$  is given by

$$\sigma^2(\rho, \phi) = \frac{1}{MN} [1 - |\psi(\rho, \phi)|^2 (2 - |\psi(\rho, \phi)|^2)] + \left( \frac{1}{M} + \frac{1}{N} \right) |\psi(\rho, \phi)|^2 (1 - |\psi(\rho, \phi)|^2). \quad (24)$$

It can be seen that at  $\rho = 0$ ,  $\sigma^2(\rho, \phi) = 0$  and away from the main-lobe,  $\sigma^2(\rho, \phi) \rightarrow \frac{1}{MN}$ , i.e., scales down as  $\frac{1}{MN}$  w.r.t. the mainlobe.

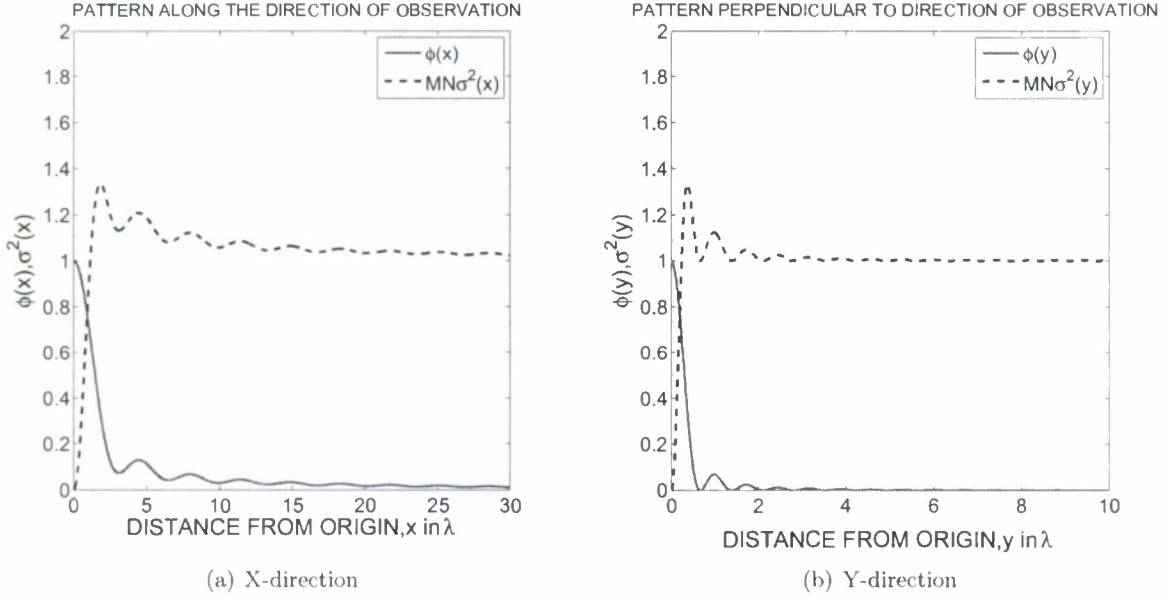


Figure 11: Cut-Pattern in X and Y directions for  $\theta_{max} = \pi/4$ ;  $M \times N$  system.

Spatial patterns of the mean and variances were computed and are shown in Figs. 11-13. Fig. 11 shows the cut-patterns of mean and variances along the  $X$  and  $Y$  directions when  $\theta_{max} = \pi/4$ . The value of variances is zero at the true location of the scatterer where the mainlobe peak occurs. Thus, the mainlobe is deterministic. As the scanning location deviates from the true scatterer location, the variance increases rapidly. In fact the variances reach a large fraction of their first peak values within the mainlobe of pattern of mean. This implies that the RPCA function becomes random within a distance in the order of a single wavelength. The variances and therefore the fluctuations can be reduced by increasing the number of antennas. With sufficiently large number of antennas, the pattern would behave similar to the pattern of mean.

Fig. 12 shows the two dimensional intensity plots of the same. The GDOP effect due to the

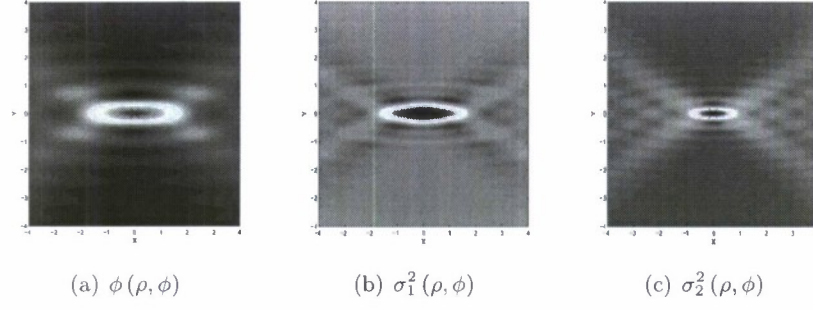


Figure 12: Two dimensional patterns for  $\theta_{max} = \pi/4$ .

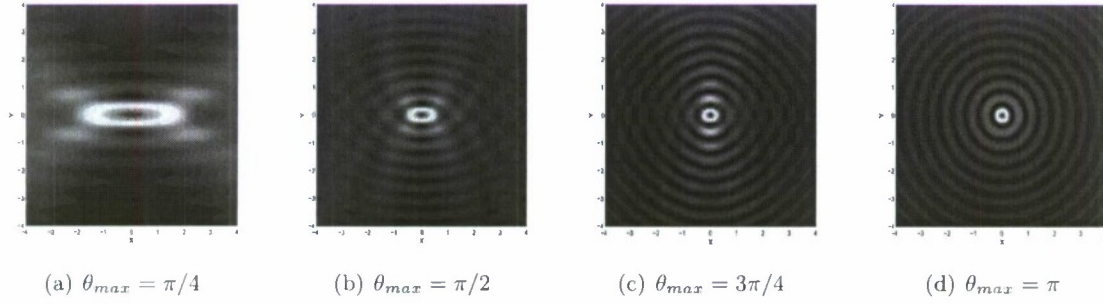


Figure 13: Two dimensional mean patterns for varying  $\theta_{max}$ .

non-symmetric placement of sensors around the target is observable in these results. Presented in Fig. 13 are the comparison of mean patterns for different values of  $\theta_{max}$ . As  $\theta_{max}$  is increased, the width of mainlobe decreases thereby increasing the resolution. Best resolution is achieved when the target is completely surrounded by the antenna field. However, the number of sidelobes within the visible area is increased as  $\theta_{max}$  is increased.

**Sensors as Transceivers** For the scenario where there are  $N$  sensors all functioning both as transmitters and receivers, there are  $N^2$  paths. However, the paths have correlations and therefore the results for  $MN$  independent paths as above change accordingly. The mean of the pattern for this scenario are as follows.

$$E[\mathcal{A}(\rho, \phi)] = E\left[\frac{1}{N^2} \left\{ \sum_{k=1}^N e^{-j2\pi(2\rho)u} + \sum_{k=1}^N \sum_{l=1, l \neq k}^N e^{-j2\pi\rho(u+v)} \right\}\right], \quad (25)$$

which leads to

$$E[\mathcal{A}(\rho, \phi)] = \frac{1}{N} \psi(2\rho, \phi) + \frac{(N-1)}{N} \psi^2(\rho, \phi), \quad (26)$$

where  $\psi(\rho, \phi) = \left[ \frac{1}{2\theta_{max}} \int_{\cos(\phi-\theta_{max})}^{\cos(\phi+\theta_{max})} \frac{e^{-j2\pi\rho u}}{\sqrt{1-u^2}} du \right]$ . The pattern variance is given by

$$\begin{aligned} \sigma^2(\rho, \phi) = & \frac{2}{N^2} - \frac{1}{N^3} + 4 \left( \frac{1}{N} - \frac{2}{N^2} + \frac{1}{N^3} \right) |\psi(\rho, \phi)|^2 - \\ & 2 \left( \frac{2}{N} - \frac{5}{N^2} + \frac{3}{N^3} \right) |\psi(\rho, \phi)|^4 - \frac{1}{N^3} |\psi(2\rho, \phi)|^2 \\ & - 2 \left( \frac{1}{N^2} - \frac{1}{N^3} \right) (\psi(2\rho, \phi)\psi^{*2}(\rho, \phi) + \psi^*(2\rho, \phi)\psi^2(\rho, \phi)). \end{aligned} \quad (27)$$

It is easily verified that at  $\rho = 0$ ,  $\psi(\cdot) = 0$  leading to  $\sigma^2(\rho, \phi) = 0$ . The behavior of mean and variance for this case is shown in Fig. 14

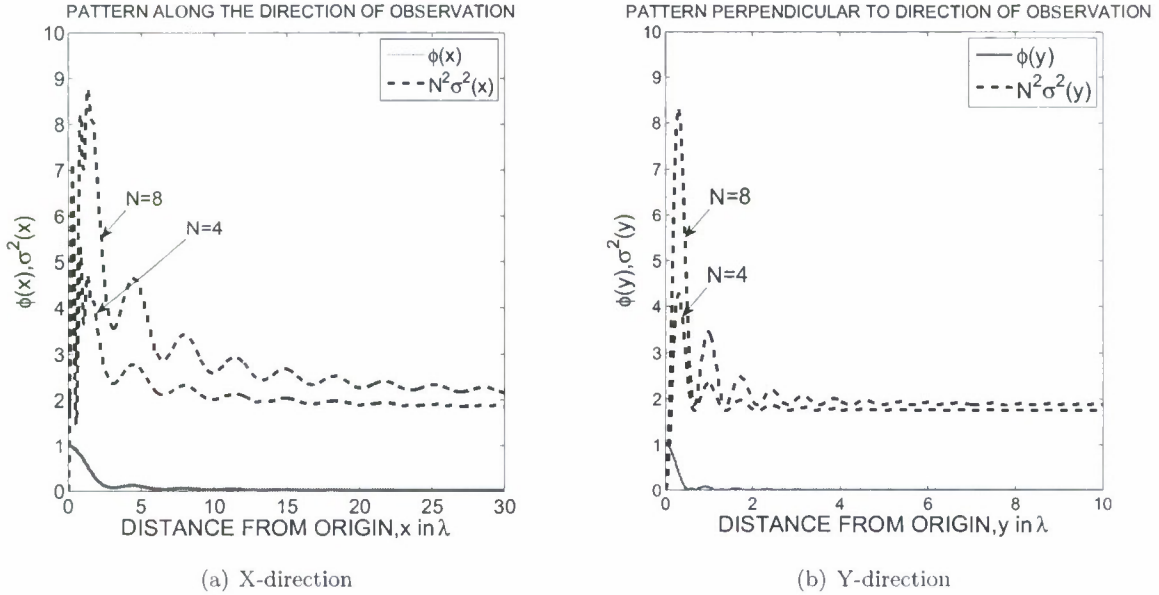


Figure 14: Cut-Pattern in X and Y directions for  $\theta_{max} = \pi/4$ ;  $N$  transmit/receive.

It is seen that for the case when each of the  $N$  antennas function both as a transmitter and a receiver, the variance converges to a value twice as much as for the case where all the antennas are independent.

**Critical Number of Antennas** While statistics such as mean and variance provide important insights on the behavior of the RPCA function, a robust design requires the sidelobe levels within the visible area to be bounded above by a tolerable value. The requirements for a given sidelobe level and a *confidence interval* are discussed in this section.

As mentioned in Section 4, the sidelobes of the RPCA function  $\mathcal{A}(\rho, \phi)$  can be modeled using the complex Gaussian distribution. From (24), it can be seen that the variance  $\sigma^2 \rightarrow \frac{1}{MN}$  for locations sufficiently far from the mainlobe. Therefore the magnitude of  $\mathcal{A}(\rho, \phi)$ ,  $Q = |\mathcal{A}(\rho, \phi)|$  has a Rayleigh probability density function given by

$$p(q) = qMN \exp\left(\frac{-MNq^2}{2}\right), \quad (28)$$

and a cumulative distribution of the sidelobe level

$$\Pr(Q \leq q) = \int_0^q p(t)dt = 1 - \exp\left(\frac{-MNq^2}{2}\right). \quad (29)$$

We are interested in determining the conditions that guarantee that most of the sidelobe peaks within the surveillance area do not exceed a specified value.

Fig. 4 shows the probability that all  $n$  independent samples of the sidelobe levels are below a given value as a function of number of antennas. In the distributed MIMO radar every antenna functions as a transmitter as well as a receiver thus  $M = N$ . It can be seen that 99% confidence level for  $-10dB$  sidelobes can be achieved with a number of antennas as low as nine. As seen from the curves for  $n = 16, 64$ , and  $256$  corresponding to surveillance area dimension of  $4, 8$ , and  $16$  wavelengths, the sensitivity of the distribution to  $n$  the number sampling points is not high.

#### 4.1 Waveform Design

Distributed coherent MIMO radar consists of randomly placed sensors over a large spatial area. Thus this radar systems inherently have the ability of high resolution as previously discussed. To keep the localization ambiguities under control, requires us to use a number of antennas larger than the threshold, as per the discussion in the previous section. The system can also benefit from optimizing the locations of antenna, which is an aspect still to be investigated. We identify that the alternative possibility is to utilize multiple sub-carriers to complement the number of sensors. The way to mitigate the sidelobes using multiple subcarriers can be demonstrated considering linear arrays and far field pattern as follows.

Let a linear array with  $M$  transmit elements. The transmit pattern as a function of angle is



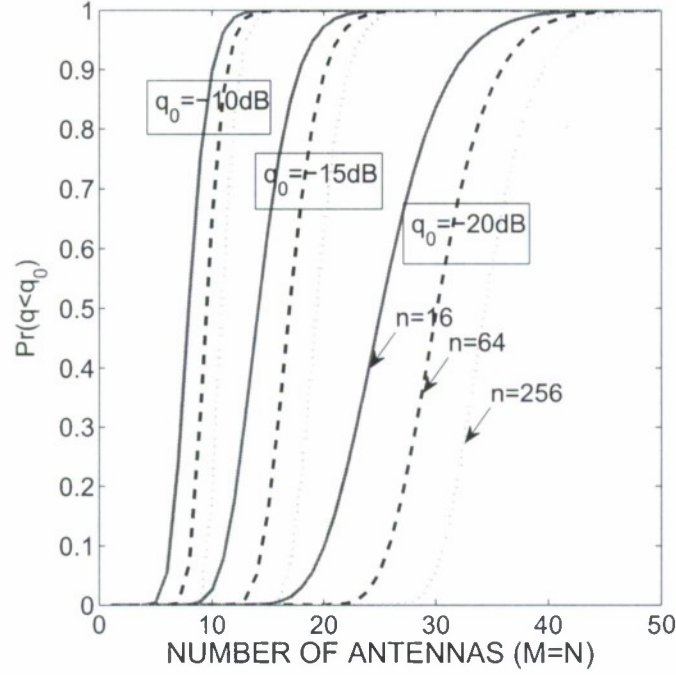


Figure 15: Distribution of sidelobe level below required target as a function of number of antennas.

given by

$$P(\theta) = \left| \sum_{m=1}^M e^{-j2\pi x_m \sin \theta} \right|,$$

where  $\theta$  is the angle with respect to the normal to the array and  $x_m$  is a sensor location expressed in terms of the nominal carrier wavelength. By plotting  $P(\theta)$  for different values of  $M$  it is possible to observe the effect of the number of sensors on the pattern. Now, let us assume that each antenna transmits  $N$  subcarriers. The pattern becomes

$$P(\theta) = \left| \sum_{n=0}^{N-1} \sum_{m=1}^M e^{-j2\pi \left(1 + \frac{f_n}{f_c}\right) x_m \sin \theta} \right|,$$

where  $f_c$  is the nominal carrier frequency and  $f_n$  is the subcarrier offset from the carrier frequency.

The phase of one of the terms in the sum above will change by  $\pi$  when

$$\frac{f_n}{f_c} x_m \sin \theta \approx 1.$$

The required frequency shift is then

$$\frac{f_n}{f_c} \approx \frac{1}{x_m \sin \theta}.$$

The pattern  $P(\theta)$  can be plotted for various values of  $M$  and  $N$ . Fig. 16 shows an example of the sidelobe reduction achieved by using multiple subcarriers. In this example, we consider 10 sensors and 256 sub-carriers.

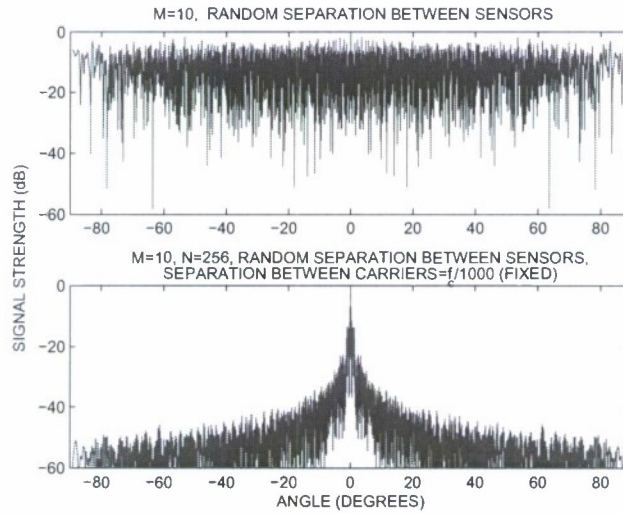


Figure 16: Sidleobe mittigation with muliple sub-carriers.

## 5 MIMO Radar Applications

This section provides several examples of MIMO radar applications, which illustrate various aspects and properties of MIMO radar. The first example illustrates the application of MIMO radar to obtain a diversity gain to overcome fades in target RCS. In the second example, multistatic observations are exploited to improve the detection capability of a moving target. The final example exploits coherent processing among the elements of MIMO radar to obtain high resolution target detection/estimation.

## 5.1 Diversity Gain

This subsection addresses radar functions that exploit RCS spatial diversity of targets. Diversity gains for target detection and direction finding are reviewed based on [23] and [36], respectively. In both cases, the target is stationary and it is observed against a background of white Gaussian noise.

### Target Detection

Diversity processing seeks to exploit multiple paths through which the signals propagate from the transmit antennas to the receive antennas. Such a path starts from a transmitter. The transmitted waveform impinges on the  $Q$  scatterers that form the target. The path terminates at a receiver, where the responses from the  $Q$  scatterers combine. Since the scatterers are too close to be resolved by the waveform, the  $Q$  echoes combine as in a flat fading multipath scenario to form a fading channel coefficient. With  $M$  transmit and  $N$  receive antennas, there are  $MN$  such paths corresponding to the  $MN$  elements of the channel matrix  $\mathbf{H}$ . Under the conditions discussed in Section 2.2 (complex targets with large  $Q$  and sufficiently spaced antennas) the  $MN$  paths are decorrelated. The set of transmitted waveforms has to be designed to facilitate the separation between waveforms arriving simultaneously at the receiver. Simple signal separation is possible when the transmitted waveforms are orthogonal and maintain their orthogonality at the receiver end.

For the target detection, we form two hypotheses: under hypothesis  $H_1$ , a target is present at  $X = (x, y)$ ; under the alternative hypothesis, the target is not present. The classic Neyman-Pearson detector is given by the likelihood ratio test

$$\log \frac{p_X(\mathbf{r}|H_1)}{p_X(\mathbf{r}|H_0)} \underset{H_0}{\overset{H_1}{\geq}} \gamma, \quad (30)$$

where  $p_X(\mathbf{r}|H_1)$  and  $p_X(\mathbf{r}|H_0)$  are the likelihood functions of the observation vectors under the respective hypotheses. The likelihood functions are parameterized by the location  $X$  of the resolution cell under test. The threshold  $\gamma$  is determined by the tolerated level of false alarms. Assuming that the components of the received vector  $\mathbf{r}(t)$  have bandwidth  $W$  (the same bandwidth as the transmitted waveforms), the density functions  $p_X(\mathbf{r}|H_1)$ ,  $p_X(\mathbf{r}|H_0)$  are understood in the conventional

sense as joint distributions of samples of the real and imaginary parts of  $\mathbf{r}(t)$  taken at  $1/W$  time intervals (see for example [35]). From the signal model (6), the observations  $r_\ell(t)$  are functions of the channel coefficients  $h_{\ell k}$ . Concatenating the columns of the channel matrix  $\mathbf{H}$  to form the length  $MN$  vector  $\mathbf{h}$ , and recalling the discussion in Section 2.2,  $\mathbf{h}$  is stochastic with probability density function  $p(\mathbf{h}) \propto \exp(-\|\mathbf{h}\|^2)$ , where  $\|\cdot\|$  denotes the Euclidean norm. This follows since the elements of  $\mathbf{h}$ , are mutually independent with each element being complex Gaussian with zero mean and variance 1. The target detection process involves the simultaneous transmission of orthogonal waveforms and the testing of a decision statistic by a central processor. The central processor is fed with data sampled by the receivers at delays corresponding to resolution cells. By suitable control of sampling instants, this process can test for the presence of a target in each of the resolution cells in Fig. 2.

Assuming orthogonality between waveforms and the signal model in (6), it is possible to extract a noisy estimate of each element of  $\mathbf{H}$  corresponding to a point  $X = (x, y)$  in the x-y plane. The estimate for element  $h_{\ell k}$  is obtained by applying the matched filter for waveform  $s_k(t)$  to the received signal at the  $\ell$ -th antenna,  $r_\ell(t)$ , and sampling at a time delay corresponding to location  $X$ :

$$y_{\ell k}(X) = \int_T r_\ell(t) s_k^*(t - [\tau_{\ell k}(X) + \tau_{r\ell}(X)]) dt. \quad (31)$$

Notice that by exploiting orthogonality between the transmitted waveforms,  $y_{\ell k}(X)$  contains the target response to only  $s_k(t)$ . Let  $\mathbf{y}(X)$  denote the vector formed by  $y_{\ell k}(X)$  for  $\ell = 1, \dots, N$  and  $k = 1, \dots, M$ . Starting with (6) and given the just described distribution for  $\mathbf{h}$ , it is possible to develop an expression for the probability density function of the received vector from a resolution cell containing the target and averaged over the values of  $\mathbf{h}$ . The detailed steps are omitted here due to space considerations, but following steps similar to those in [23], it can be shown that

$$\begin{aligned} p_X(\mathbf{r}|H_1) &= \int_{\mathbf{h}} p_X(\mathbf{r}|H_1, \mathbf{h}) p(\mathbf{h}) d\mathbf{h} \\ &\propto \exp\left[-\frac{1}{\sigma_w^2} \left(\int_T \|\mathbf{r}(t)\|^2 dt\right)\right] \exp\left[\frac{\|\mathbf{y}(X)\|^2}{\sigma_w^2 (\sigma_w^2 + \frac{E}{M})}\right]. \end{aligned} \quad (32)$$



For hypothesis  $H_0$ , we have

$$p(\mathbf{r}(t)|H_0) \propto \exp \left[ -\frac{1}{\sigma_w^2} \left( \int_{\mathcal{T}} \|\mathbf{r}(t)\|^2 dt \right) \right]. \quad (33)$$

It follows that the Neyman-Pearson detector is given by

$$\begin{array}{c} H_1 \\ \|\mathbf{y}(X)\|^2 \geq \gamma_1. \\ H_0 \end{array} \quad (34)$$

In order to set the value of the threshold  $\gamma_1$  for a tolerated level of false alarms, the central processor has to have full model knowledge, i.e., the values of waveform energy  $E$  and noise power  $\sigma_w^2$ . By inspection of (34), the optimal processor is a non-coherent combiner of the signals pre-processed by the sensors. With  $M$  transmitters and  $N$  receivers and under conditions discussed earlier,  $\|\mathbf{y}(X)\|^2$  is the sum of the magnitudes of  $MN$  uncorrelated noisy estimates of channel coefficients. When, with suitable normalization, a single term  $|y_{\ell k}(X)|^2$  has a  $\chi_2^2$  (chi-square with two degrees of freedom) distribution, the test statistic in (34) has the improved statistical properties of a  $\chi_{2MN}^2$  random variable.

Closed-form performance expressions are given in [23] for cases with full and partial model knowledge. The figure reproduced here is for the case that the signal energy and noise power level are known. Fig. 17 illustrates the gains provided by MIMO radar (curves labeled “MIMO”) over a conventional phased-array radar (labeled “conv”). The curves in the figure represent the miss probability as a function of SNR for a fixed false alarm probability of  $10^{-6}$  and for various MIMO/phased-array configurations. The slopes of the MIMO curves clearly show diversity gains similar to those obtained in communications (compare to [27] for example). For a more extensive set of results we refer the reader to [23].

### **Direction Finding**

Another application that can benefit from the diversity gain of MIMO radar is direction finding (DF). In this case, the target spatial diversity is supported by widely separated transmitters, while the receiving sensors are placed at  $\lambda/2$  intervals to enable unambiguous DF. Such a system is studied in [36]. Here, we reproduce some of the numerical results from [36]. The mean square error

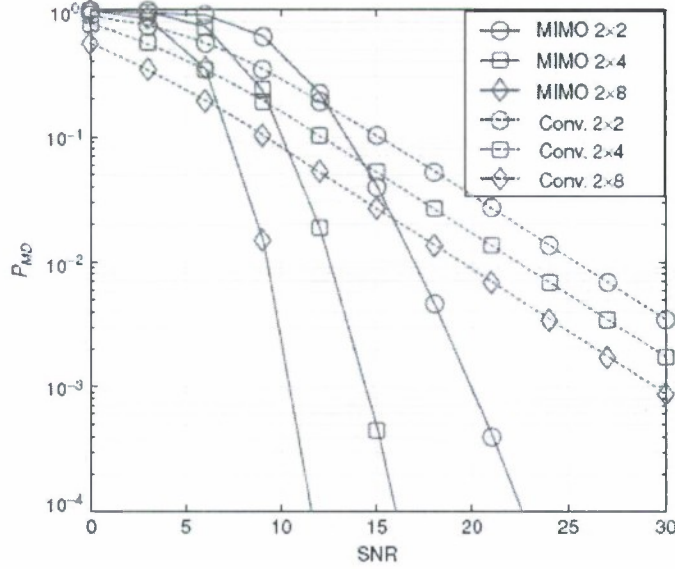


Figure 17: Miss probability of MIMO radar compared to conventional phased-array. Miss probability is plotted versus SNR for a fixed false alarm probability of  $10^{-6}$ .

(MSE) of the maximum likelihood (ML) estimate of the angle of arrival is evaluated and plotted versus the SNR for various antenna configurations. Fig. 18 shows the MSE for number of transmit antennas  $M = 1, 2, 4$ , and  $16$ , respectively. The target is located at boresight,  $\theta = 0$ , and the phased array at the receiver utilizes  $N = 6$  elements. It is observed that the MSE for the single-antenna case,  $M = 1$ , is much larger than for  $M = 4$  or  $M = 16$ . MIMO radar transmit diversity with  $M = 4$  provides a gain of more than 20 dB for the same MSE.

## 5.2 Moving Target Detection

Observing targets over wide angular sectors with a MIMO radar offers great benefits for Doppler processing and moving target detection (MTD). MIMO radar is particularly useful in some cases when the targets are difficult to distinguish from the background clutter. The enhanced MTD performance of MIMO radar stems from its distributed nature, which makes it possible to overcome typical problems that plague conventional or array radars such as targets with low radial velocities or blind speeds. Further, the joint processing of the received waveforms results in superior performance compared to multistatic radar, where each sensor typically performs its own Doppler shift

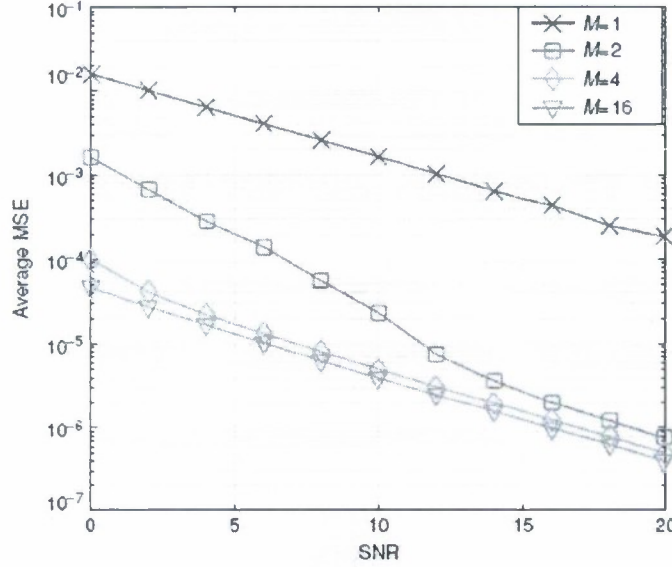


Figure 18: Average MSE of the ML estimator versus SNR.

estimation.

MTD with MIMO radar is investigated in [24]. The scenario considered consists of a single transmitter and  $N > 1$  widely dispersed receivers. The transmitter and receivers are stationary. It is assumed that the moving target is sufficiently far from the sensors such that its Doppler shift with respect to the sensors is constant during the observation of  $K$  samples. A central processor is fed with test statistics computed at the sensors. The clutter is assumed zero-mean, complex Gaussian with known  $K \times K$  temporal covariance matrix  $\mathbf{C}$ . The clutter is also assumed spatially homogeneous in the sense that it has the same properties for all transmitter-receiver pairs and for all resolution cells. In Section 2.1, in discussing target detection, the channel elements  $h_{\ell k}$  were modeled as stochastic with known statistics. Here, we take a slightly different approach, and assume that these coefficients are deterministic unknown. The two slightly different approaches follow the respective models employed in the references that are reviewed in this paper, but should not affect key features of MIMO radar.

In this subsection, tests for the detection of a single, moving target are discussed. The target, if present, is moving with unknown velocity components  $(v_x, v_y)$ , where  $v_x$  and  $v_y$  are deterministic,

unknown velocities measured in an arbitrary Cartesian coordinate system (refer to Fig. 6 for an illustration of the setup). Given  $M$  transmitters and  $N$  receivers, there are  $MN$  paths resulting in  $MN$  different spatial looks at the resolution cell under test. The same number of looks can be obtained with a single transmitter and  $MN$  receivers; hence, to simplify notation, and without loss of generality, the discussion below assumes  $M = 1$ . In Fig. 19, the locations of the transmitter and the receiving sensors are denoted respectively,  $T_1$  and  $R_\ell$ ,  $\ell = 1, \dots, N$ . The target and the transmitter are aligned on the  $x$  axis, while the receivers form angles  $\theta_\ell$  with the target-transmitter axis.

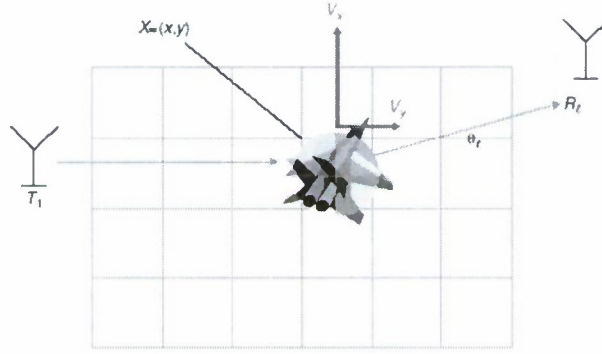


Figure 19: Moving target detection scenario: single transmit antenna at location  $T_1$ , multiple receive antennas at locations  $R_\ell$ , making angles  $\theta_\ell$ ,  $\ell = 1, \dots, N$ . Target at  $X = (x, y)$  with velocity components  $v_x$ ,  $v_y$ .

To test for the presence of the target in a resolution cell, we develop a generalized likelihood ratio test (GLRT). The GLRT maximizes the likelihood ratio test over the unknown parameters: the target response  $h_{\ell k}$  and the velocities  $v_x$ ,  $v_y$ . Under hypothesis  $H_1$ , a target is present in the tested resolution cell centered at coordinates  $X = (x, y)$ ; under the alternative hypothesis, the target is not present in the resolution cell. A vector  $\mathbf{y}_\ell(X)$  is defined to consist of  $K$  time samples of the form  $y_{\ell 1}(X)$  defined in (31), and taken at the pulse repetition interval,  $T_{\text{PRI}}$ . The GLRT is evaluated by first expressing the likelihood ratio as a function of the unknown parameters  $h_{\ell k}$ ,  $v_x$ , and  $v_y$ . Subsequently, the likelihood ratio is maximized over the unknown parameters. Skipping



the details of the analysis, we list the MTD decision rules obtained for three types of radar: MIMO radar, multistatic radar, and phased array radar:

The GLRT decision rule for MIMO radar is

$$\max_{v_x, v_y} \sum_{\ell=1}^N \frac{|\mathbf{d}^\dagger(f_\ell) \mathbf{C}^{-1} \mathbf{y}_\ell(X)|^2}{\mathbf{d}^\dagger(f_\ell) \mathbf{C}^{-1} \mathbf{d}(f_\ell)} \underset{H_0}{\overset{H_1}{\geq}} \gamma_2, \quad (35)$$

where  $\mathbf{d}(f_\ell)$  is a  $K \times 1$  vector representing the matched filter to a target response with Doppler frequency  $f_\ell$ . This vector is composed of  $K$  time samples taken at the pulse repetition intervals,  $T_{\text{PRI}}$ , and it has the form

$$\mathbf{d}(f_\ell) = [1, \exp[-j2\pi f_\ell T_{\text{PRI}}], \dots, \exp[-j2\pi f_\ell (K-1) T_{\text{PRI}}]]^T, \quad (36)$$

where  $f_\ell$  is the Doppler shift due to the motion between the sensor and the target. The Doppler shift can be evaluated with the help of Fig. 6, and it is given by

$$f_\ell = \frac{v_x}{\lambda} (1 + \cos \theta_\ell) + \frac{v_y}{\lambda} \sin \theta_\ell. \quad (37)$$

For example, for a target moving along the  $x$  axis with velocity  $v_x$  towards the transmitter and receiver, the Doppler shift is comprised of the frequency shift due to the motion between transmitter and target ( $v_x/\lambda$ ), and the frequency shift due to the target-receiver motion ( $(v_x/\lambda) \cos \theta_\ell$ ). Finally, the threshold  $\gamma_2$  is determined by the tolerated level of false alarms. Notice that the test statistic in (35) is computed for each resolution cell  $X$  represented by a square in Fig. 19. The location  $X$  of the resolution cell determines the values of angle  $\theta_\ell$  needed in (37) and the values of  $\mathbf{y}_\ell(X)$  computed using (31). A test statistic is computed at each sensor such that the clutter spectrum is whitened. The optimal processor is a non-coherent combiner of the test statistics computed at each sensor. The aggregate statistic is maximized over values of  $v_x, v_y$  velocities and the result is compared to the threshold  $\gamma_2$  to decide on the target presence.

Moving on to the multistatic radar, each sensor performs its own estimation of the Doppler shift  $f_\ell$  rather than the joint processing carried out by the MIMO radar. This means that rather

than finding estimates  $v_x$ ,  $v_y$  and restricting  $f_\ell$  to the form in (37), each sensor estimates  $f_\ell$  that maximizes a statistic computed locally. Then, the decision rule is

$$\sum_{\ell=1}^N \max_{f_\ell} \frac{|\mathbf{d}^\dagger(f_\ell) \mathbf{C}^{-1} \mathbf{y}_\ell(X)|^2}{\mathbf{d}^\dagger(f_\ell) \mathbf{C}^{-1} \mathbf{d}(f_\ell)} \underset{H_0}{\overset{H_1}{\geq}} \gamma_3, \quad (38)$$

where  $\mathbf{d}(f_\ell)$  is still defined by (36), but  $f_\ell$  does not have to obey (37).

Finally, the performance of the phased array is limited by its small aperture. Lacking the ability to view the target from multiple aspects, the phased array can observe only a single Doppler shift,  $f_\ell = f$ . The  $N$  transmit elements are beamformed to provide coherent processing gain. The GLRT decision rule is then given by

$$\max_f \frac{|\mathbf{d}^\dagger(f) \mathbf{C}^{-1} \mathbf{y}(X)|^2}{\mathbf{d}^\dagger(f) \mathbf{C}^{-1} \mathbf{d}(f)} \underset{H_0}{\overset{H_1}{\geq}} \gamma_4, \quad (39)$$

where  $\mathbf{y}(X)$  is the vector of  $K$  time samples at the output of the beamformed array corresponding to a target at  $X$ .

The receiver operating characteristics (ROC) of the three different types of radar systems: the MIMO radar from (35) (labeled “MIMO”), the multistatic radar from (38) (‘MS’), and the array radar from (39) (‘conv’) are shown in Fig. 20. Parameters used in the simulations include  $T_{\text{PRI}} = 0.5$  ms,  $K = 10$  samples, carrier frequency = 1 GHz, clutter-to-noise ratio = 30 dB, and target angle of arrival  $0^\circ$ . There are  $N = 8$  receiving sensors placed at uniformly spaced angles in the sector  $-40^\circ$  to  $50^\circ$  with respect to the target. The target velocity is 300 km/h with random direction. The curves are parameterized by the target-to-clutter ratio (‘tc’).

The results demonstrate the superiority of MIMO radar over multistatic or array radars. The advantage over multistatic radar stems from the joint processing that constrains the search to velocities  $(v_x, v_y)$  common to all sensors. An additional advantage of MIMO radar is the ability to exploit the spatial diversity of RCS values. The multistatic radar can also benefit from RCS diversity, but since Doppler processing is local, it yields higher false alarms. The increase in false

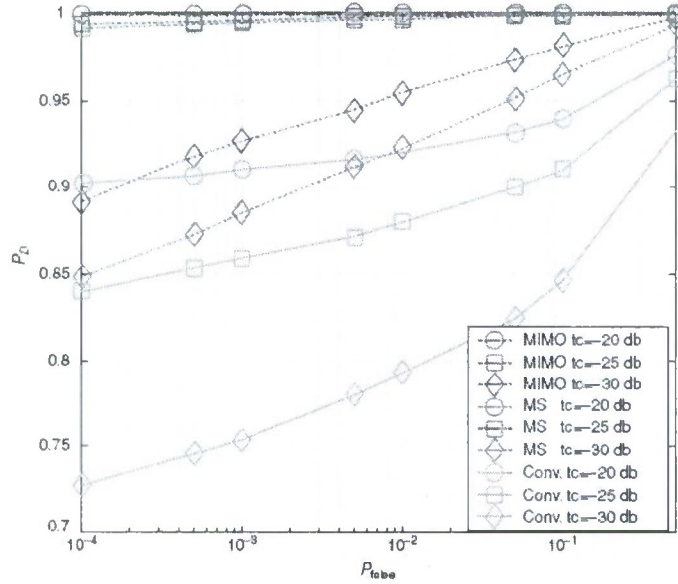


Figure 20: ROC for a 300 km/h target with random direction and with RCS fluctuations.

alarms accounts for the gap in performance. The phased-array radar is handicapped by both low Doppler response to low radial velocities and by RCS fading.

## 6 Conclusions

In this report, we introduced the concepts of MIMO radar and reviewed some recent work focusing on applications with widely dispersed antenna elements. Generally speaking, MIMO radars transmit multiple waveforms, receive signals at multiple antennas, and process them jointly. Processing may be carried out non-coherently (as in Sections 2.1 and 2.2) or coherently (as in Section 2.3).

The main topics discussed in the paper can be summarized as follows:

- Complex targets contain a large number of scatterers that result in diverse RCS patterns as a function of angle. Decorrelation of the elements of the channel matrix occurs for complex targets and widely separated antennas.
- For a target with spatially diverse backscatter, optimal processing of MIMO radar with suitably located sensors leads to diversity gains in the form of improved statistics of the SNR. The

processing collects the energy reflected by the scatterers and combines it non-coherently.

- MIMO radar can locate targets with high resolution and can resolve between closely spaced targets. The processing for high resolution location beamforms the transmitted and the received signals to achieve resolution on the scale of the carrier wavelength. High resolution target location is challenged by ambiguity sidelobes and the need to phase synchronize a multisite radar system.

- MIMO radar with a hybrid architecture of widely distributed transmitting sensors and a phased array receiver provides diversity gains for direction finding.

- Observations over a wide angular sector can be exploited to detect targets moving in arbitrary directions.

MIMO radar with widely separated sensors is a very promising concept for future, high performance radars. Yet many research and engineering challenges need to be addressed to advance MIMO radar from concept to reality. Engineering challenges include: centralized coordination of sensor transmissions, synchronized communication with a processing center, and highly precise phase synchronization among sensors (of the order of nanoseconds for resolutions in meters). Research challenges include a better understanding of bistatic and multistatic RCS phenomena, tracking targets with MIMO radar, MIMO radar on airborne platforms, and others.

## References

- [1] H. Godrich, A. M. Haimovich and R. S. Blum, Concepts and Applications of A MIMO Radar System with Widely Separated Antennas, Book chapter to be published by Wiley (2007)
- [2] H. Godrich, A. M. Haimovich, and R. S. Blum Target Localization Techniques and Tools for MIMO radar IEEE Radar Conference, May 2008.
- [3] H. Godrich, A. M. Haimovich, and R. S. Blum Mapping the Lower Bound on Localization Accuracy for coherent MIMO Radar Systems ICASSP, April 2008.
- [4] E. Brookner, "Phase arrays around the world - progress and future trends," *IEEE International Symposium on Phased Array Systems and Technology*, pp.1 - 8, Oct. 2003.
- [5] L. Swindlehurst and P. Stoica, "Maximum likelihood methods in radar array signal processing," *Proc. of the IEEE*, vol. 86, pp. 421-441, Feb. 1998.



- [6] S. Haykin, J. Litva, and T. J. Shepherd, *Radar Array Processing*, New York: Springer-Verlag, 1st ed., 1993.
- [7] A. Farina, *Antenna Based Signal Processing Techniques for Radar Systems*, Norwood, MA: Artech House, 1992. Science Publishers, 1998.
- [8] L. E. Brennan and I. S. Reed, "Theory of adaptive radar," *IEEE Trans. on Aerospace and Electronic Systems*, vol. AES-9, March 1973, pp. 237-252.
- [9] J. Ward, "Space-time adaptive processing for airborne radar," in *Proc. of the IEEE National Radar Conference*, 1995, pp. 2809-2812.
- [10] W. L. Melvin, "A STAP overview," *IEEE Aerospace and Electronic Systems Mag.*, vol. 19, Jan. 2004, pp. 19-35.
- [11] R. Klemm, *Principles of Space-Time Adaptive Radar*, IEE Press, 2002.
- [12] J. R. Guerci, *Space-Time Adaptive Processing for Radar*, Norwood, MA: Artech House, 2003.
- [13] V.S. Chernyak, *Fundamentals of Multisite Radar Systems*, Gordon and Breach, 1998.
- [14] J. M. Colin, "Phased array radars in France: Present and future," in *Proc. of the IEEE Int. Symp. on Phased Array Systems and Technology*, Oct. 1996, pp. 458-462.
- [15] A. S. Fletcher and F. C. Robey, "Performance bounds for adaptive coherence of sparse array radar," in *Proc. of the 11th Conf. on Adaptive Sensors Array Processing*, March 2003.
- [16] D. W. Bliss and K. W. Forsythe, "Multiple-input multiple-output (MIMO) radar and imaging: degrees of freedom and resolution," in *Proc. of 37th Asilomar Conference on Signals, Systems and Computers*, Nov. 2003, pp. 54-59.
- [17] D. Rabideau, "Ubiquitous MIMO digital array radar," in *Proc. of 37th Asilomar Conf. on Signals, Systems, and Computers*, Nov. 2003, pp. 1057-1064.
- [18] E. Fishler, A. Haimovich, R. Blum, L. Cimini, D. Chizhik, and R. Valenzuela, "MIMO radar: An idea whose time has come," in *Proc. of the 2004 IEEE Int. Conf. on Radar*, April 2004, pp. 71-78.

- [19] D.R. Fuhrmann and G. San Antonio, "Transmit beamforming for MIMO radar systems using partial signal correlation," in *Proc. of 38th Asilomar Conf. on Signals, Systems and Computers*, Nov. 2004, pp. 295-299.
- [20] F. C. Robey, S. Coutts, D. Weikle, J. C. McHarg, and K. Cuomo, "MIMO radar theory and experimental results," in the *38th Asilomar Conference on Signals, Systems and Computers*, November 2004, pp. 300-304.
- [21] I. Bekkerman and J. Tabrikian, "Target detection and localization using MIMO radars and sonars," *IEEE Trans. on Sig. Proc.*, vol. 54, Oct. 2006, pp. 3873- 3883.
- [22] L. Xu, J. Li, and P. Stoica, "Adaptive techniques for MIMO radar," *14th IEEE Workshop on Sensor Array and Multi-channel Processing*, Waltham, MA, July 2006.
- [23] E. Fishler, A. Haimovich, R. Blum, L. Cimini, D. Chizhik, and R. Valenzuela, "Spatial diversity in radars - models and detection performance," *IEEE Trans. on Sig. Proc.*, vol. 54, March 2006, pp. 823-838.
- [24] N. Lehmann, A. M. Haimovich, R. S. Blum, and L. Cimini, "MIMO-radar application to moving target detection in homogenous clutter," *14th IEEE Workshop on Sensor Array and Multi-channel Processing*, Waltham, MA, July 2006.
- [25] N.H. Lehmann, A.M Haimovich , R.S. Blum, L.J.Cimini, "High Resolution Capabilities of MIMO Radar," in *Proc. of 40th Asilomar Conf. on Signals, Systems and Computers*, Nov. 2006.
- [26] G. J. Foschini, "Layered space-time architecture for wireless communication in a fading environment when using multiple antennas," *Bell Labs Technical Journal*, vol. 1, no. 2, pp. 41-59, 1996.
- [27] V. Tarokh, N. Seshadri, and A. Calderbank, "Space-time codes for high data rate wireless communication: Performance criterion and code construction," *IEEE Trans. on Info. Theory*, vol. 44, March 1998, pp. 744-765.

- [28] E. Fishler, A. Haimovich, R. Blum, L. Cimini, D. Chizhik, and R. Valenzuela, "Performance of MIMO radar systems: advantages of angular diversity," in *Proc. of 38th Asilomar Conf. on Signals, Systems and Computers*, Nov. 2004, pp. 305-309.
- [29] M. Skolnik, *Introduction to Radar Systems*, 3rd ed., New York: McGraw-Hill, 2001.
- [30] Y. Yang and R.S. Blum, "Radar waveform design based on mutual information and mean-square error estimation," to be submitted to *IEEE Trans. on Aerospace and Electronic Systems*.
- [31] I. Papoutsis, C. J. Baker, and H. D. Griffiths, "Fundamental performance limitations of radar networks," in *Proc. of 1st EMRS DTC Technical Conf.*, Edinburgh, 2004.
- [32] R. Viswanathan and P. K. Varshney, "Distributed detection with multiple sensors I: Fundamentals," *Proc. of the IEEE*, vol. 85, Jan. 1997, pp. 54-63.
- [33] R. S. Blum, S. A. Kassam, and H. V. Poor, "Distributed detection with multiple sensors II: Advanced topics," *Proc. of the IEEE*, vol. 85, Jan. 1997, pp. 64-79.
- [34] R. S. Blum, "Distributed detection for diversity reception of fading signals in noise," *IEEE Trans. on Inf. Theory*, vol. 48, Jan. 1999, pp. 158-164.
- [35] P. M. Woodward, *Probability and Information Theory with Application to Radar*, Norwood, MA: Artech House, 1953.
- [36] N. Lehmann, E. Fishler, A. M. Haimovich, R. S. Blum, D. Chizhik, L. Cimini, and R. Valenzuela, "Evaluation of transmit diversity in MIMO-radar direction finding," *IEEE Trans. on Sig. Proc.*, accepted.
- [37] N. Lehmann, *Some Contributions on MIMO Radar*, Ph.D. Dissertation, New Jersey Institute of Technology, 2006.
- [38] B. D. Steinberg, "The peak sidelobe of the phased array having randomly located elements," *IEEE Trans. on Antennas and Propagation*, vol. AP-20, March 1972, pp. 129-136.
- [39] B. D. Steinberg, *Principles of Aperture and Array System Design*, John Wiley 1976.
- [40] H. Godrich, A. M. Haimovich, and R. S. Blum, "Cramer Rao bound on target localization estimation in MIMO radar systems," *CISS*, March 2008.

- [41] H. Godrich, A. M. Haimovich, and R. S. Blum, "Target localization accuracy gain in MIMO radar based system," to be submitted to *IEEE Trans. on Sig. Proc*
- [42] Y. Lo, "A mathematical theory of antenna arrays with randomly spaced elements," *IEEE Transactions on Antennas and Propagation*, vol. 12, No. 3, pp. 257-268, May 1964.
- [43] B. D. Steinberg and E. H. Attia, "Sidelobe reduction of random arrays by element position and frequency diversity," *IEEE Trans. on Antennas and Propagation*, vol. AP-31, Nov. 1982, pp. 922-930.